COMPUTATIONAL MODELING OF BIOFILM FORMATION AND CORROSION PROCESSES ON STEEL SURFACES

A Thesis

by

MARK DAVID WATERS JR.

Submitted to the Office of Graduate and Professional Studies of
Texas A&M University
in partial fulfillment of the requirements for the degree of

MASTER OF SCIENCE

Chair of Committee,	Maria King
Committee Members,	Ronald Lacey
	Reza Sadr
Head of Department,	Steve Searcy

May 2020

Major Subject: Biological and Agricultural Engineering

ABSTRACT

The oil and gas industry is in constant search of ways to decrease the losses due to corrosion issues. Although the process of corrosion has been studied extensively, there is very little information available regarding the factors that affect microbially influenced corrosion. For that reason, this research project is aiming at filling in this gap of knowledge. The purpose of this study is to determine the microbially influenced corrosion on metallic surfaces in hydraulic oil fracturing and create computational models for the formation of biofilms.

To conduct this experiment, stainless steel type 304 coupons were used. The coupons were placed in different environments within the flow system: some coupons were left untreated (not exposed to fracturing water), some placed in the fresh fracturing water in a stationary state, and the rest of the coupons were placed in a dynamic flow with the fracturing water. All of the coupons were exposed in an incubator to a constant temperature of 70 Celsius for more accurate results when comparing them to real-world situations. Each week coupons were taken out of the chamber so the surfaces could be imaged and analyzed using Atomic Force Microscopy in conjunction with Analysis System Workbench software.

The results showed that coupons in a stationary state will corrode at a faster rate than coupons in a dynamic flow. Untreated coupons will only exhibit minor changes over time. The faster rate could have been due to more salts incorporating into the biofilm on the surface of the stationary coupons leading to an increase in weight. This was expected because weight was an independent variable that determined the outcome for the rate of corrosion. The overall trend for biofilm formation on stainless steel was visualized by atomic force microscopy and the image analysis allowed for the creation of a predictive computational model to show how corrosion will form on the surface of metals.

DEDICATION

This work is dedicated to the oil and gas professionals who are in constant search of ways to solve this rising issue. Hoping that this study will contribute to the corrosion mitigation technologies in oil industry, I am looking forward to collaborating with you all to help minimize corrosion costs.

ACKNOWLEDGEMENTS

I would first like to thank my committee chair Dr. King. I am forever grateful for your unwavering support, scholastic wisdom, and constant motivation throughout the entirety of this research.

Special thanks to my graduate committee members Dr. Lacey and Dr. Sadr for their advice and guidance. I greatly appreciate the support.

I also would like to thank and acknowledge Dr. William Serem for his assistance and expertise in conducting image analysis.

Many thanks to my fellow lab mates Gabriela Ramos, Tatiana Baig, and Hyoungmook Pak for their help with the analytical methods.

Lastly, I would like to thank all my friends and family for their encouraging words and high faith in me to be great. Without them, none of this would have been possible.

CONTRIBUTORS AND FUNDING SOURCES

Contributors

This work was supervised by a thesis committee consisting of Dr. Maria King (advisor) and Dr. Ronald Lacey of the Department of Biological & Agricultural Engineering and Dr. Reza Sadr of the Department of Mechanical Engineering.

All work conducted for the thesis was completed by the student independently.

Funding Sources

This graduate study was supported the Texas A&M System Louis Stokes Alliance for Minority Participation fellowship program.

NOMENCLATURE

2D	Two-Dimensional
3D	Three-Dimensional
AFM	Atomic Force Microscopy
ANSYS	Analysis System
CFD	Computational Fluid Dynamics
DNA	Deoxyribonucleic Acid
ICP-MS	Inductively Coupled Plasma Mass Spectrometry
MATLAB	Matrix Laboratory
MIC	Microbially Influenced Corrosion
PVC	Polyvinyl Chloride
QIIME	Quantitative Insights Into Microbial Ecology

TABLE OF CONTENTS

Page

LIST OF FIGURES

Page

LIST OF TABLES

Page

1. INTRODUCTION

The oil and gas industry needed a comprehensive study for corrosion and biofilm formation. Billions of dollars are spent annually on replacing corroded pipes and equipment. Methods to decrease the economic impact of losses are limited due to this commonly recurring issue. For that reason, the main purpose of this project was to develop a predictive computational model based on the dynamic changes in the surface biofilm of stainless-steel coupons exposed to back-produced fracturing water. This research is important because the oil industry experiences various forms of corrosion. It is difficult to determine ways to reduce corrosion without knowing its mechanism. Therefore, monitoring the formation of biofilm and its microbiome and determining its elemental composition were key steps in creating a model that could help in finding techniques to decrease the corrosion rate. The use of our measurement techniques in combination with modeling software packages may offer a solution to this problem.

1.1. Background

Corrosion costs the world economy around $2.2 trillion a year which is approximately 3 percent of the world's Gross Domestic Product (2002). Of that $2.2 trillion, $1.372 billion are oil industry related costs. Almost 70 percent of all oil and gas wells developed are highly corrosive mostly resulting in surface corrosion in pipelines. The gained knowledge and techniques used in this study will allow for the improvement of preventive techniques for corrosion buildup.

The study of biofilm growth has become more and more prevalent in any field that examines the integrity of materials. A biofilm is the assembly of microbial cells that attach themselves to surfaces (Lewandowski and Beyenal 2003). This assembly could be a single species or a diverse group of species. These biofilms form on various types of surfaces such as pipes,

medical devices, rocks, etc. It was interesting to find that some biofilms contain nutrients that help the environment while they can also cause corrosion.

In this experiment, there are many physical properties that are expected to change due to exposure to the fracturing water. The major property will be mass. Because there will be corrosion present, it will cause the mass of each steel coupon to vary based on how long it is exposed to fracturing water at high temperatures. Some other properties that will increase because of this is length, width, and height of the biofilm. It was expected that a stationary state will cause these physical properties to increase more quickly than in a more dynamic flow. Density will also play an important role because it is directly related to the mass of the steel.

1.2. Literature Review

Corrosion on metals creates many problems in the workforce. Carbon steel, chromium, nickel, manganese, Inconel, etc. are all metals used in industry that are not withstanding due to their corrosive nature (Popoola et al. 2013). These metals are exposed to temperatures between 30ºC and 200ºC on average, or even higher based on industry needs. Because of this, companies continuously try to find ways to reduce the corrosion rate of the metals. This is important because when the useful life of materials increases, companies will have an increase in revenue because parts and equipment will not need to be purchased or replaced as often.

1.2.1. Types of Corrosion

In the oil and gas industry, multiple types of corrosion can occur. Although they all are key factors in the industry's spending, the most common corrosion types associated with the industry and this study included surface, pitting/galvanic, and microbially influenced corrosion.

1.2.1.1. Surface Corrosion

Surface corrosion occurs when an electrical or electrochemical reaction breaks down the surface of an exposed metal, causing it to weaken and ultimately fail. This form of corrosion is the most common because most metals are constantly in contact with environmental effects including humidity, temperature variations, acidic fluids, etc. that can lead to issues. Figure 1.1 displays an example of what the appearance of surface corrosion can be.

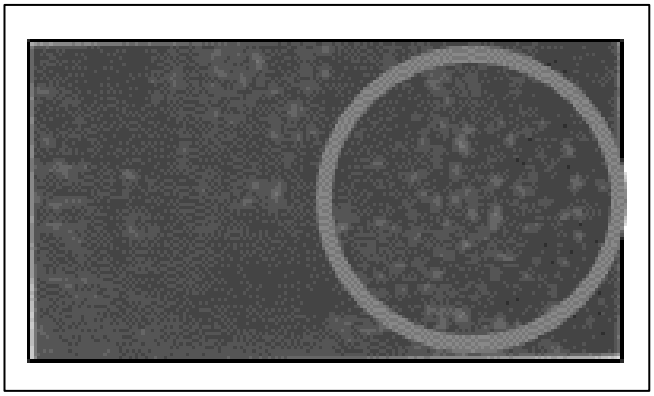

Figure 1.1 *Example of surface corrosion. It shows how the surface is deteriorating through the corrosion forming on the surface of the steel.*

1.2.1.2. Pitting/Galvanic Corrosion

Pitting corrosion, shown in Figure 1.2, is the most severe type of corrosion in the oil industry. This is largely due to the fact that it is extremely hard to detect, and it grows rapidly (Nanan 2018). Because of the high temperatures and pressures along with the oil flowing through the steel pipes, it causes weak points in the steel pipes which, in turn, leads to detrimental corrosion (Hakkarainen 2003). Pitting costs the oil and gas industry billions of dollars annually because it is so big in every aspect of exploration and production.

Galvanic corrosion occurs when two different metals are in contact with each other in the presence of an electrolyte. This situation results in metals that have a lower or most negative potential corroding because it has become the anode (Popoola et al. 2013). In doing this, the flow

of electrons become balanced because the anode begins to lose its metal ions. This form of corrosion is also shown in Figure 1.2.

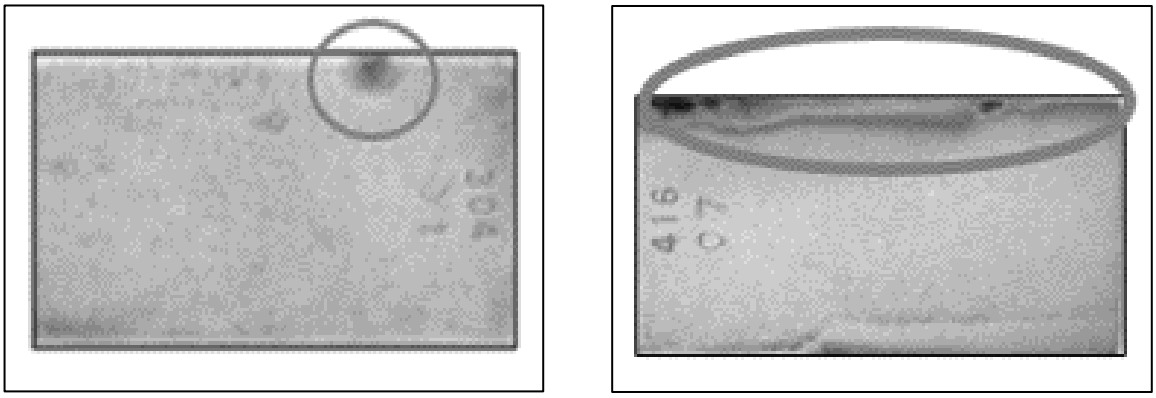

Figure 1.2 *Examples of pitting (left) and galvanic (right) corrosion. On the left image, a pit began to form because there was a specific area of focus. The right image shows how steels will react when contacted with another steel or metal in the surrounding area.*

1.2.1.3. Microbially Influenced Corrosion

MIC occurs when microbial organisms release hydrogen sulfide and carbon dioxide onto a surface. This increases the toxicity and corrosivity of a well or pipeline (Zhang et al. 2015). It is categorized as slimy deposits on the inside of pipe walls. It is said that normally pitting corrosion is a result of microbially influenced corrosion. MIC usually starts to form between the temperatures of 10ºC and 50ºC when the material is carbon steel, stainless steel, copper, or aluminum. To reduce MIC, companies either clean their metals regularly, use chemicals to reduce the growth rate, or completely drain the mechanical systems. It is believed that placing emphasis on biofilm formation will ultimately help to mitigate the severe MIC issues in the oil and gas industry (Eckert 2015). The process of MIC is shown in Figure 1.3.

The process goes through five stages over the course of its formation: the lag phase, the exponential growth phase, the decreasing rate phase, the plateau phase, and the sloughing phase (Bryers and Characklis 1982). The lag phase refers to the attachment of the biofilm and how it

begins to form a microcolony of the surface it has attached itself to. From there, the biofilm begins to grow exponentially forming a subpopulation interaction on the surface. This is when the biofilm looks like mucus or slime. Next, it enters the decreasing rate phase where the biofilm is still growing but the process is slowing down at a specific rate forming a macrocolony, a secondary colonization. The biofilm then enters the plateau phase. This is when the biofilm has formed into a mature biofilm thus causing it to reach its corrosive potential and continuously attack the surface. Lastly, the biofilm enters the sloughing phase which is where the biofilm begins to detach itself from the surface in order to form new biofilm in different areas to repeat this process. These cells disperse based upon the effects of the flow (Donlan 2002).

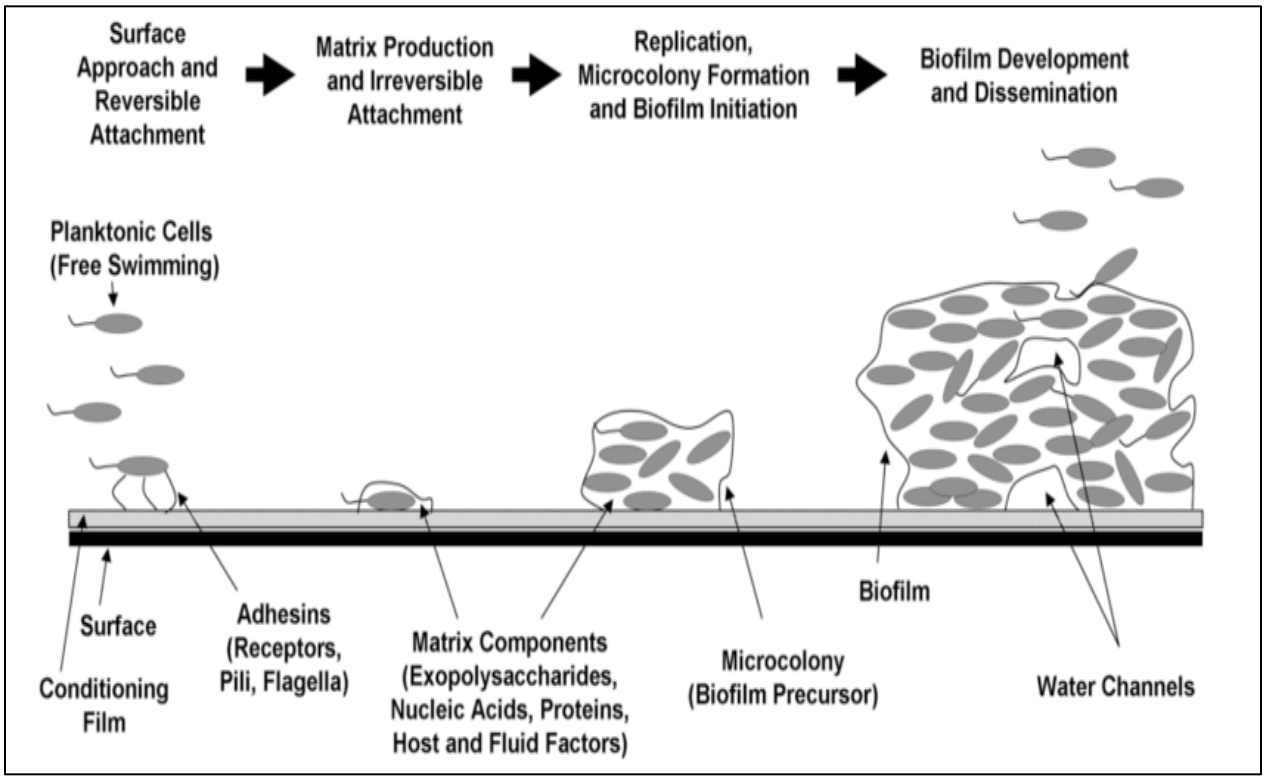

Figure 1.3 *Example of MIC. It shows the process of how MIC attaches itself to the surface, grows, and lastly spreads onto the rest of the surface of the metal (Cadieux et al. 2008).*

1.2.2. Fracturing Water

Fracturing is the process of drilling or injecting a fluid at a high pressure into the surface of the earth to release oil and gas (Clark 1949). Companies use water to help a maximize the fracturing process. This contaminates the water, hence, "fracturing water". Fracturing water contains many elements that are harmful to metals as well as the environment such as lead, mercury, arsenic, etc. (Yari 2017). These chemicals increase toxicity and corrosivity as well. From earlier, we know that this harms the metals that they come in contact with. Figure 1.4 shows some of the corrosive elements that were present in the fracturing water used for this study.

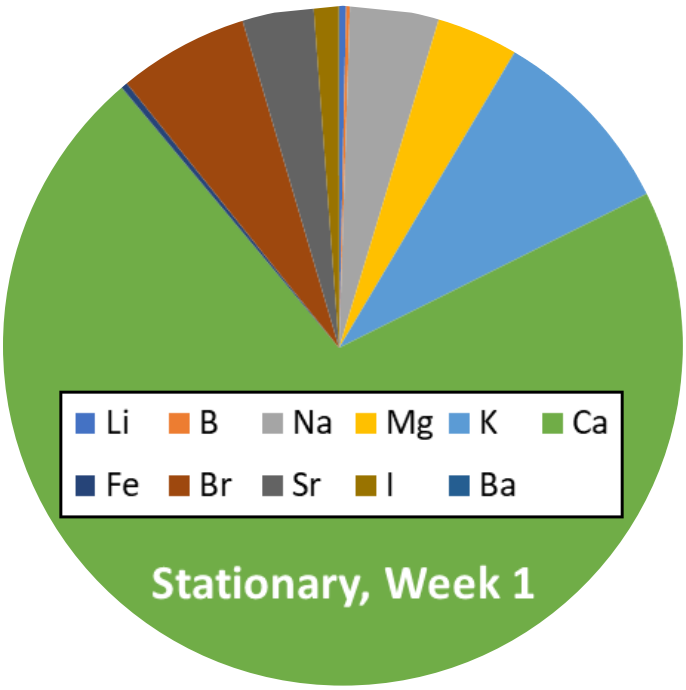

Figure 1.4 *The common corrosive elements found in hydraulic fracturing water. These elements caused heavy biofilm development in this study.*

1.2.3. Previous Work

Techniques to create 3D models of these build-ups are challenging due to their dynamic fluctuations. This is largely due to the fact that the parameters of the bacteria are so small. Models have been made using 3D particle tracking velocimetry and imaging devices such as a micro x-ray

diffraction. Also, there was a breakthrough when a group of professors combined their knowledge in their respective fields utilizing computational fluid dynamics, numerical simulations, and visualizations to model their experiment. They were able to obtain some parameters using the calculated variables: inlet velocity, Reynold's number, the microbial flow rate, porosity, cross-sectional area, and the average size of the grain used in the experiment (Peszynska et al. 2016). An example of their work using ANSYS software is shown below in Figure 1.5. This study is slightly different because it used regular water for analysis which made it easier to monitor the corrosion build up. Because fracturing water was used for this research study, the monitoring techniques had to be altered.

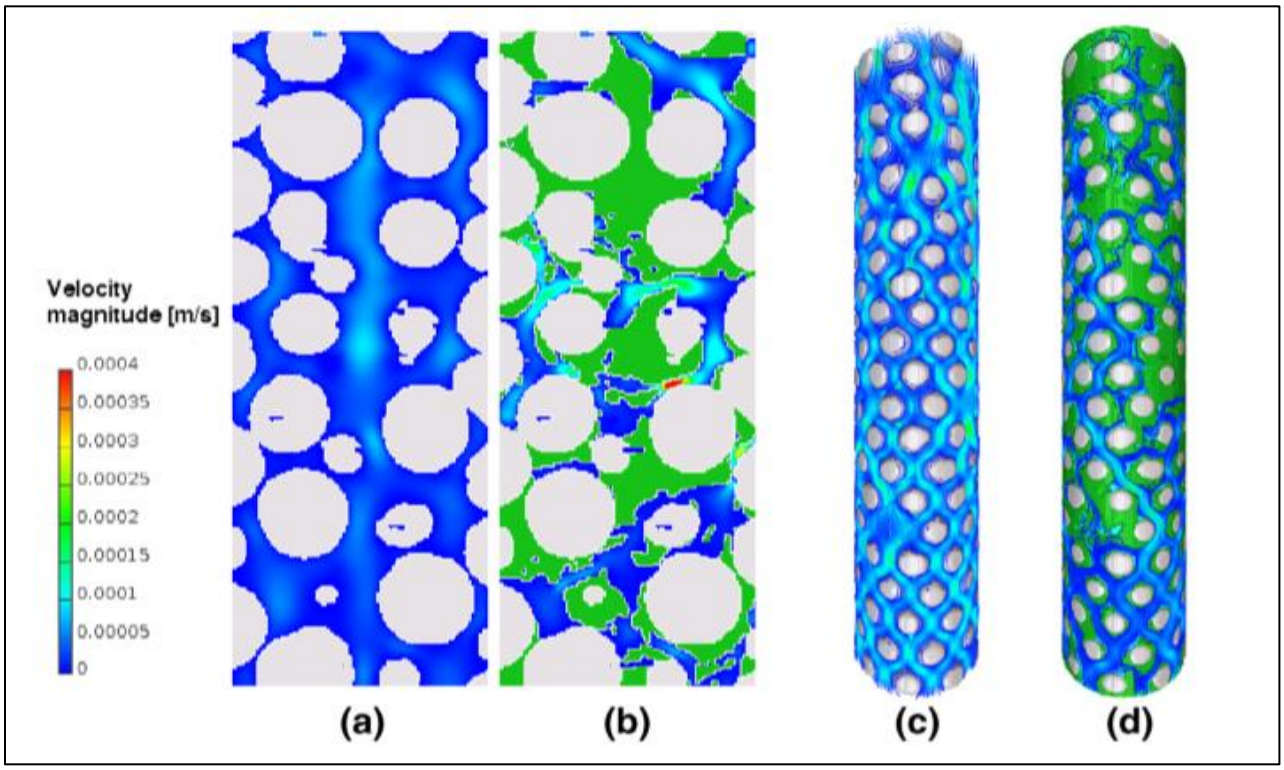

Figure 1.5 *Advances in Water Resources Example. The simulation results display: (a) magnitude of velocities without biofilm, (b) magnitude of velocities with biofilm, (c) the flow streamlines without biofilm, and (d) the flow streamlines with biofilm (Peszynska et al. 2016).*

1.3. Relevant Equations between Variables

For this study, there were three principal equations utilized for consideration: corrosion rate, Hooke's Law, and Reynolds number. These equations all were vital for the completion of this project. The equations in this section will show a correlation between the independent and dependent variables of the experiment.

1.3.1. Corrosion Rate

The most familiar technique was to ensure that the weights for the samples were recorded before and after exposure to the fracturing water. Upon doing this, the weights were divided by the total exposure time and specified area of interest. The following equation was then used to determine the corrosion rate in mm/yr (Umeozokwere et al. 2016):

$$\boldsymbol{R_{corr} = \frac{K \cdot \Delta W}{\rho_{steel} \cdot A \cdot T}} \qquad (1)$$

where,

R_{corr} *= Corrosion rate (mm/yr)*

K = Constant for unit conversion (87.6)

ΔW = Change in weight (g)

ρ_{steel} *= SS 304 density (g/mm*^{3}*)*

A = Surface area of sample (mm^2*)*

T = Time of exposure (yrs)

The uncertainty in the corrosion rate equation assumed that the surface area remained constant throughout the course of the experiments and the corrosion rate was uniform over the entire surface of the coupons. Though common, this method for estimating corrosion rate on steel was seen as effective when conducting analysis on the samples. It aided in finding trends in the

data as well as comparing the untreated, stationary, and dynamic flow coupons' mass changes and biofilm formation.

1.3.2. Hooke's Law

One of the many benefits for using atomic force microscopy was its ability to perform precise force measurements in desired regions on samples. This force was calculated by applying Hooke's Law:

$$\boldsymbol{F = -k_c d} \qquad (2)$$

where,

F = Force between tip and sample (N)

k_c = Stiffness of cantilever tip (N/m)

z = Deflection of the cantilever (m)

The equation shows a relationship between forces the applied to a spring and its elasticity (Vishalashi 2017). This law is essentially used for materials or objects that are within their elasticity limits. It states that the strain of an object s directly proportional to its applied stress as shown in the equation above. This is the governing equation used for systems with a spring-like component. When using the AFM, this force remained constant for all samples. This allowed for more accurate results when comparing the profiles of the biofilm buildup.

1.3.3. Reynolds Number

The Reynolds number equation works to describe complex flows in different environments. It helps to provide more accurate turbulence models for simulations. For flow through a pipe or tube, this number is defined as:

$$\boldsymbol{N_{Re} = \frac{\rho_{fluid} \cdot V \cdot D}{\mu}} \qquad (3)$$

where,

N_{Re} *= Reynolds number*

ρ_{fluid} *= Density of the fluid (kg/m*^{3}*)*

V = Averaged velocity of the fluid (m/s)

D = Inner diameter of the pipe (m)

μ *= Viscosity of the fluid (kg/m·s)*

Using this number allowed for the characterization of the flow regime whether laminar of turbulent (Uruba 2018). It is the ratio of inertial forces to viscous forces. This number usually remains constant throughout the system unless there is a sudden change in velocity or diameter. For a fully developed laminar flow, this number is typically less than 2300, while for turbulent flow, it is greater than 4000. Values between 2300 and 4000 are said to be a transient flow.

1.4. Objective(s)

The intention of this project was to contribute the knowledge of how to minimize corrosion related expenses through visualization. More specifically, it assisted in determining how stainless-steel 304 alloy coupons would react with constant exposure to produced water and heat over specified time periods. Compiling image files using CFD analysis assisted in the implementation of a coded script for simulating biofilm formation on steel surfaces. The desired measuring technique combined with proper simulation methods was explored to aid in reducing the corrosion rate on steel. The objectives of this study were as follows:

1) Prepared an experimental setup to monitor the process of corrosion,
2) Analyzed biofilm development with atomic force microscopy
3) Visualized and modeled the biofilm dynamic changes, and
4) Analyzed the fracturing (frac) water and biofilm microbiome composition

1.5. Hypothesis

The overall goal of this research was to reduce the corrosion rate on steel surfaces in order to extend the life of the materials. Through preliminary analysis, it was expected that constant exposure to fracturing water would cause steel to corrode at a more rapid pace based on its surrounding environment, as shown in Figure 1.6.

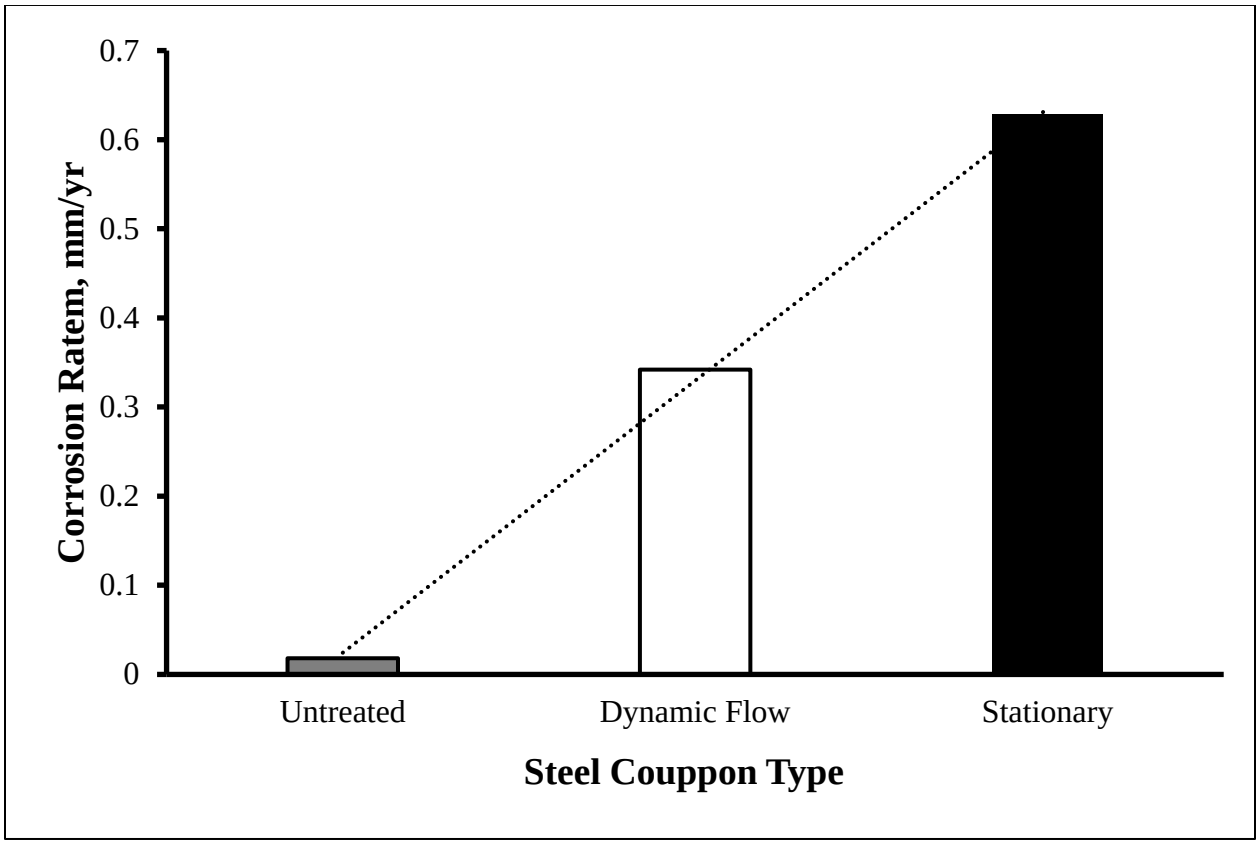

Figure 1.6 *Expected results for the corrosion of the samples. A higher corrosion rate was anticipated for the steel coupons that are in the stationary flow.*

2. MATERIALS AND METHODOLOGY

In this chapter, the experimental apparatus, measurement techniques, and methodology for conducting analysis will be described in detail. The instruments needed for the completion of this experiment were an AFM and weighing scale. The AFM was used to image the surface of the coupons and the scale was be used to determine the sample's change in mass. ANSYS software was also needed to 3D model the biofilm buildup. This allowed for the development of a multimodal imaging representation for the dynamic changes in the biofilm over time.

2.1. Experimental Setup

To conduct this experiment, stainless steel type 304 coupons were used. Each of the coupons were placed in one of three environments: some left untreated (not exposed to fracturing water), some placed in fracturing water in a stationary state, and some placed in a dynamic flow with the fracturing water. All of the coupons remained in a heating chamber in their specific environments at a constant temperature of 70^{o}C for more accurate results when compared to real-world downhole conditions. The overall setup is shown in Figure 2.1.

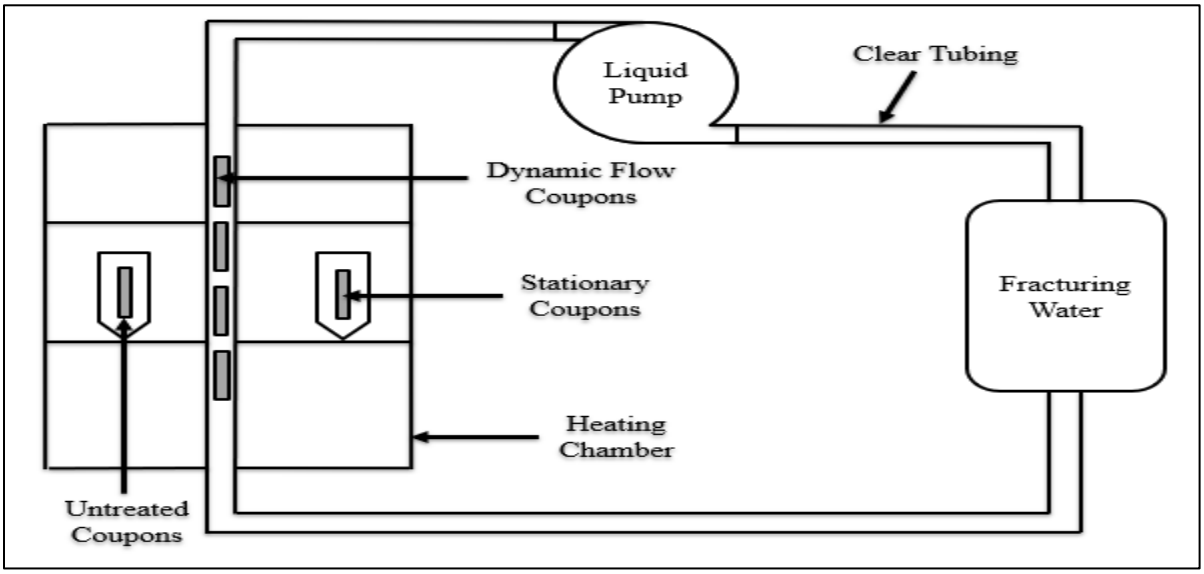

Figure 2.1 *The experimental setup for the project. It displays the materials used and the flow process for the fracturing water.*

2.1.1. Experimental Parameters

Over the course of the experiments, there were multiple things that had to remain constant. Table 2.1 shows the specifications of the equipment used for the project. The steel coupons had to be slightly smaller in width in order for them to fit inside of the clear tubing. The openings for the tubing had to be able to completely cover the inlet and outlet of the pump. This is why the PVC material was chosen. It was flexible, chemical resistant, and able to withstand a maximum of 74°C. Furthermore, some constraints for the experiment are listed below. These were important to know because each one of them could have affected the results obtained from the experiments.

Table 2.1 *Main Equipment Specifications*

Liquid Pump	Stainless Steel Type 304 Coupons	PVC Clear Tubing
Flow Rate: 37.9 L/min	Length: 50.8 mm	Inner Diameter: 25.4 mm
Inlet Diameter: 25.4 mm	Width: 22.86 mm	Outer Diameter: 31.25 mm
Outlet Diameter: 25.4 mm	Height: 0.4765 mm	Length: 6096 mm

Experimental Constraints:

- Coupons in a flow system: A flow (laminar or turbulent) was needed around the steel coupons so that the results were relatable to realistic conditions (i.e. oil rigs).
- Maintained a sterile environment: The system was kept in this type of environment because it was less prone to contamination by other microorganisms.
- Fresh fracturing water with live bacteria: Recycled fracturing water contains different chemical compounds than that of fresh fracturing water because recycled water has been exposed to corrosive metals already. This could have affected the fracturing water composition.
- Standard use steel coupons: This experiment was primarily based on time; therefore, the coupons were the same in order to accurately monitor the buildup.

- Multimodal Approach: Several methods were necessary for this study because it is difficult to conduct the experiments with a single approach.

2.1.2. Experimental Procedure

There was a specific process needed for preparing and conducting the experiments. These steps had to be followed thoroughly to ensure safety and accuracy of results. The experimental procedure was as follows:

1. Each steel coupon was labeled.
2. The steel coupons were weighed using the digital weighing scale. The results were recorded.
3. The clear tubing was placed inside of the heating chamber.
4. Some of the steel coupons were placed inside the clear plastic tubing (dynamic flow coupons). The others were placed in two separate containers, leaving some untreated and some surrounded in fracturing water (stationary). They were not in a flow.
5. The liquid pump was then connected to the clear tubing. Special attention was given to ensuring that there are no gaps in the connection.
6. The clear tubing surrounding the dynamic flow coupons was filled with produced water until no air present in the system.
7. The liquid pump was turned for an hour every day for one week to allow the fracking water to flow around the coupons.
8. After the week passed, one of the steel coupons was removed out of the tubing along with an untreated and stationary coupons. The system had to remain off during this process.
9. Each steel coupon was weighed, and the results were recorded.

10. The coupons were then placed in separate containers and taken to the Materials Characterization Facility for image analysis.
11. Each coupon was placed, one by one, on the sample surface of the AFM.
12. The AFM was given time to produce a visual image of the topography of each coupon.
13. The surface roughness and average height of the biofilm was recorded.
14. Once the image was produced, the 2D image was converted into a 3D image.
15. The 3D image was imported into the Space Claim modeler in ANSYS.
16. A dynamic mesh was placed over the imaged sample in ANSYS using the meshing function.
17. The coupons were put inside a container and placed in a freezer.
18. This process was repeated for each coupon, in one-week intervals, until all samples were imaged and analyzed.
19. Once all images were collected, MATLAB used to create a simulation to show how the biofilm formed and shaped over the course of the experiments.
20. A microbiome analysis was conducted on the coupons and the fracking water to determine their elementary content.

2.2. Assessment of Chemical and Physical Properties

In this section, the chemical and physical properties of the steel coupons will be discussed in depth to help fully understand the methods used to determine the elemental content of the biofilm. The elemental composition of the biofilm build-up was only done for the stationary and dynamic flow coupons because the untreated coupons were not exposed to the fracturing water. Atomic Force microscopy is also included in this section. All coupons were scanned and examined to determine their respective surface changes.

2.2.1. Gravimetry for the Steel Coupons

For the record of mass changes in the steel coupons, the weight for each sample was taken before they were exposed to back-produced water and after. This was needed because mass is directly related to the corrosion rate. The recorded weights were used to determine how fast biofilms built on the surfaces of the samples.

2.2.2. ICP-MS Elemental Composition

The total elemental composition was analyzed by inductively coupled plasma mass spectroscopy on a Perkin Elmer Nexion 300D spectrometer (Perkin Elmer, Waltham, MA) according to the EPA method 6010C.

Preliminary analysis of the elemental composition of the back-produced fracturing water showed high levels of alkaline and alkaline earth metals in all of the stationary and dynamic flow samples. Interestingly, higher levels of sodium, however, a magnitude lower levels of potassium, calcium, magnesium, iron, bromine, iodine and strontium were detected in the samples associated with dynamic flow compared to the stationary samples. This is supported by Figure 3.2.

2.2.3. Atomic Force Microscopy Image Examination

The main measuring technique used in this experiment was Atomic Force Microscopy. An AFM is a measuring device that images surfaces on a nanoscale. It uses a physical probe tip to scan almost any desired specimen. Using Hooke's law, the AFM can measure the "attractive and repulsive forces acting between the atoms of a sharp tip and those of the sample's surface" (Gavara 2017). It has three main abilities: force measurement, imaging, and manipulation. Its main components include a cantilever, laser, photodetector, scanner, z feedback, and a probe tip. These are shown in Figure 2.2 below. Once the experiments were completed, each sample was analyzed individually at the same orientation and location. All image analysis was conducted in the Material

Characterization Facility using the Icon AFM. To produce the image of the specimens, it took 3 stages. The first stage was sensing. In this process, the force between the tip and the sample was created by way of the tip moving closer to the sample. The next stage was detection. In this stage, the deflection of the cantilever was monitored and all of the changes in deflection were recorded by the photodetector. The last stage was imaging which is where the image is sent to the computer for analysis. The region of interest was of scan size 40 µm by 40 µm. Though this was only a small area of the coupon, it gave a probable idea of what the surface looks like as a whole.

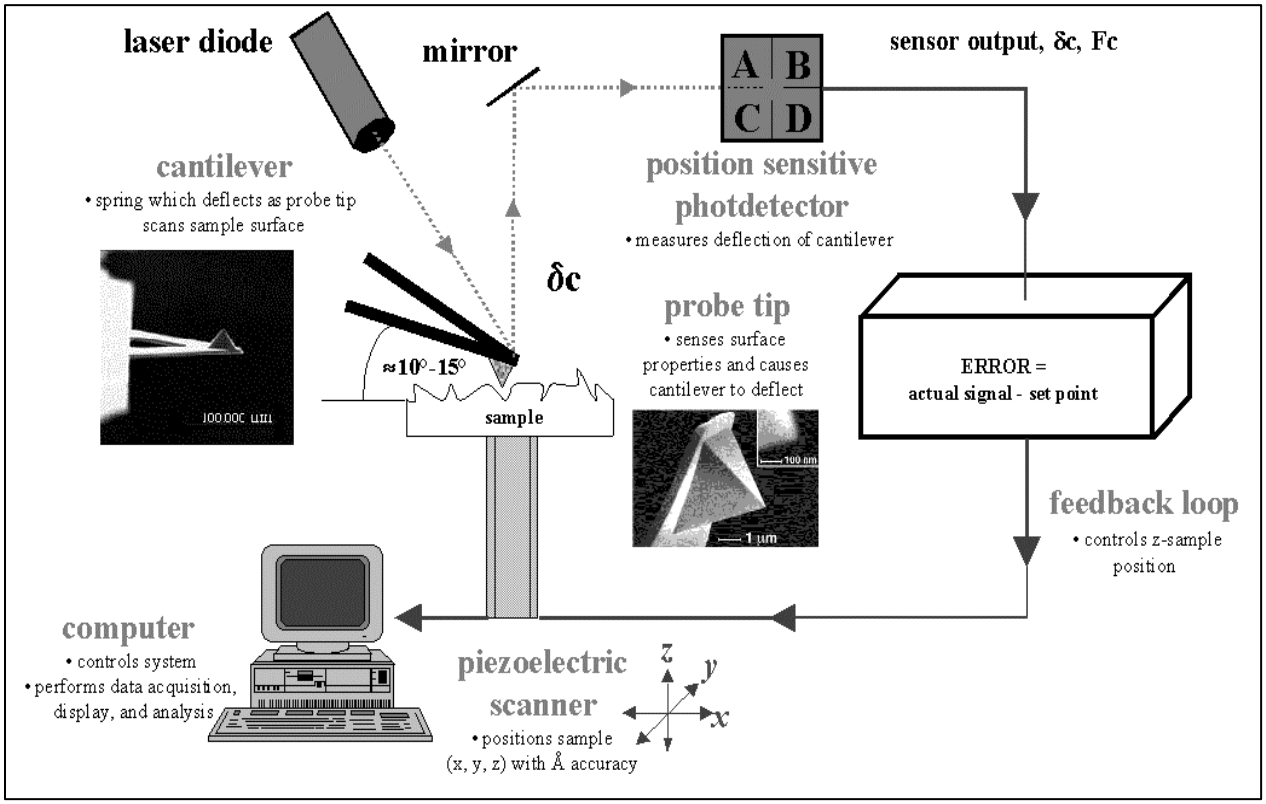

Figure 2.2 *Components of an AFM. A brief description is given for their respective functions (Ravindran 2016).*

2.3. Examination of Sample Meshing and Simulation

This section details the methods used for the creation of 3D models for the simulation of the steel coupons' biofilm development. ANSYS in concurrence with MATLAB allowed for

effective corrosion analysis. These approaches to simulation assisted in projecting how biofilms would form on the surface of steels based off their surrounding environments. Without this essential method of examination, the research project would not contribute to filling the gap in corrosion studies.

2.3.1. Computational Model of Meshing

To develop the mesh over the 3D image samples, ANSYS was utilized for precision. ANSYS is a software used to analyze various systems such as structural, thermal, and electromagnetic. There are essentially three major steps for a full, accurate analysis of a desired structure or sample. First, a geometry is created and uploaded for optimization. Next, a finite element model is appropriately setup in order to complete the last phase, solving. Once the model is solved, the geometry is examined for limitations and strong points.

A triangular dynamic mesh was placed on each of the imaged samples to enhance the severity of the biofilm build-up. The mesh size was consistent throughout for exactness when comparing results. The figures in section 3.4 show how the mesh looked for each of the coupons. Notice that the orientations were the same. This allowed for there not to be any skewness of results.

2.3.2. Animation of Biofilm Formation

Once all of the images were compiled, a proper simulation was designed to understand the trend of the biofilm formation throughout the course of the experiments. For this project, MATLAB was used to construct a code that captures the images for each system (i.e. untreated, stationary, and dynamic flow) from start to finish. The code was written to transform the MATLAB file into a .mp4 file. This displayed a real-time animation of how the biofilms developed onto the surfaces of the coupons. From there, trends in the formation were determined and the profile observed. The script for the animation visibly showed each coupons' growth over time.

2.4. Molecular Composition of the Biofilm

This section includes the methods on how the biofilm DNA was extracted and analyzed.

2.4.1. DNA Extraction

The Alkaline Lysis method was used to extract DNA from all the samples (Zhou et al., 1990). The DNA concentration was determined by measuring optical density at 260 nm (OD_{260}) using a spectrophotometer (NanoDrop Technologies, Inc., Wilmington, Del.).

2.4.2. Illumina Sequencing and Biofilm Microbiome Composition

Bacterial DNA recovered from the bioaerosol samples were analyzed at the Genomic Sequencing and Analysis Facility (GSAF) at the University of Texas at Austin (Austin, Tex.) for Illumina® paired-end (2×250) sequencing on the MiSeq platform. First-round PCR was used to amplify the V4/V5 regions of the 16S rRNA gene using the primers 515F (5'-GTGYCAGCMGCCGCGGTA-3') (Baker et al., 2003) and 909R (5'-CCCCGYCAATTCMTTTRAGT-3') (Wang and Qian, 2009).

2.4.2.1. QIIME Statistical Analysis

Bacterial DNA sequences were processed and analyzed in the open-source bioinformatics pipeline "Quantitative Insights Into Microbial Ecology" v.1.8 (Caporaso et al., 2010). Sequences were demultiplexed and forward and reverse reads were merged using FLASH v.1.2.11 (Magoč and Salzberg, 2011) with a maximum overlap of 250 bp. Sequences were quality-filtered (-q 19), and chimeras were removed via QIIME and USEARCH (Edgar, 2010). High-quality sequences were clustered into operational taxonomic units (OTUs) at 97% similarity using QIIME's USEARCH-based open-reference OTU clustering workflow (pick_open_reference_otus.py). Global singleton OTUs were removed. All samples were rarefied to the least number of sequences present in any individual sample as is commonly done in microbiome studies. Taxonomy was

assigned using the Ribosomal Database Project classifier (Wang et al., 2007) with the reference database Greengenes13_8 16s rRNA (McDonald et al., 2012) for bacteria.

2.5. Biofilm Kinetics

The attached biofilm rate was studied in this project in order to evaluate how the biofilm reacted during specific time periods. The method for finding this rate was found by using the equation:

$$\frac{\partial \beta}{\partial t} = R_g + R_d - R_r \quad (4)$$

where,

β = Attached biofilm rate

R_g = Net biofilm production rate

R_d = Deposition rate of the suspended biofilm

R_r = Detachment rate of the biofilm

In calculating the attached biofilm rate, multiple parameters had to be considered based upon the overall effect they had on the steel coupons. Each of the parameters were computed by dividing mass by the surface area and time. Surface area remained constant throughout all computations because all coupons were the same size. Time was adjusted based upon the number of hours the coupons were exposed to the heat and fracturing water. Mass was also modified because each rate was based on a different parameter. The net biofilm production rate was computed by using the change in mass of the coupons, the deposition rate was found by utilizing the mass of the calcium ions present on the coupons' surface, and the detachment rate used the mass of the potassium ions. These masses all had a major impact on the biofilm's development on the coupons' surface.

3. RESULTS AND DISCUSSION

This chapter includes the discussion of results obtained from the research study. All outcomes from the experiments and modeling were necessary in making the research valuable. The results helped to fill the gap in current corrosion studies and gave insight as to how to predict biofilm growth when designing equipment.

3.1. Gravimetry

Below are the tables (3.1, 3.2, and 3.3) for the recorded weights of the steel coupons before and after they were exposed to fracturing water. The untreated coupons were the only weights that slightly decreased over time because they were corroding without exposure. For the dynamic flow and stationary coupons, the weights increased each week due to being exposed to different elements contained in the fracturing water. This was interesting to find because normally corrosion cause weight to decrease. It is as if the different elements are packing themselves onto the surface of the coupons and staying attached. Microbially influenced corrosion was the type of corrosion experienced in the experiments because the process for attachment and detachment was the same.

Table 3.1 *Untreated Coupons Weights Before and After Exposure*

Exposure (wks)	Before Exposure Weight (g)	After Exposure Weight (g)
1	47.9231	47.9226
2	47.9231	47.9221
3	47.9231	47.9118
4	47.9231	47.9111
8	47.9231	47.9025
12	47.9231	47.9016
16	47.9231	47.9009
20	47.9231	47.9005
24	47.9231	47.8993

Table 3.2 *Stationary Coupons Weights Before and After Exposure*

Exposure (wks)	Before Exposure Weight (g)	After Exposure Weight (g)
1	47.9480	48.124
2	47.9480	48.1325
3	47.9480	48.1526
4	47.9480	48.1842
8	47.9480	48.2514
12	47.9480	48.2584
16	47.9480	48.3159
20	47.9480	48.3362
24	47.9480	48.3371

Table 3.3 *Dynamic Flow Coupons Weights Before and After Exposure*

Exposure (wks)	Before Exposure Weight (g)	After Exposure Weight (g)
1	48.6341	48.6745
2	48.5800	48.6483
3	47.8991	48.0241
4	48.0523	48.1853
8	48.0459	48.1854
12	47.9970	48.1657
16	47.7375	47.9104
20	47.7946	48.0578
24	47.6939	47.9721

Figure 3.1 shows the overall change in weight, loss or gain, in the coupons. From the results, it was clear that the stationary coupons had the overall highest increase in weight.

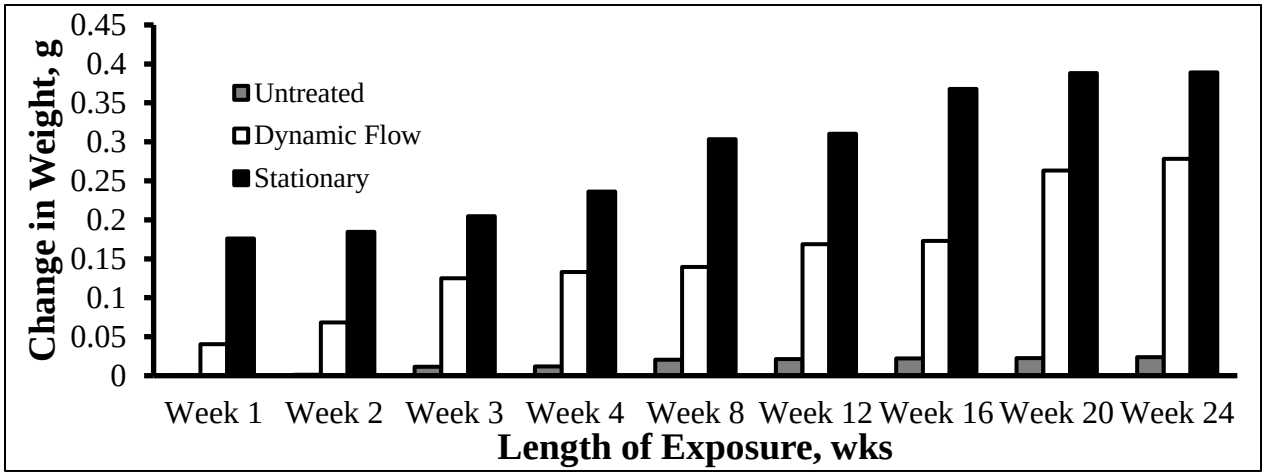

Figure 3.1 *Changes in the weight of the coupons. The graph shows the exposed conditions (i.e. untreated, dynamic flow, and stationary) over the time period of 191 days.*

3.2. ICP-MS

In Table 3.4, it gives the numeric values for the concentrations of each element that was present on the surface of the coupons. The units for the values are ng/mL. The "S" in the table indicates that the analyte signal was too high to quantify. The values correspond to $1/40^{th}$ of biofilm on each coupon dissolved in 10 mL of 1% nitric acid by a 25.4 mm by 25.4 mm area.

Table 3.4 *Elemental Composition of Biofilm for Dynamic Flow and Stationary Coupons*

Analyte	**Week 1**	**Week 1**	**Week 8**	**Week 8**	**Week 24**	**Week 24**
	Flow	**Stationary**	**Flow**	**Stationary**	**Flow**	**Stationary**
Li	59	904	34	529	55	929
B	211	478	201	394	215	512
Na	S	11480	S	14812	S	7749
Mg	944	10487	395	6179	828	10414
K	3353	24858	2112	18079	2917	25290
Ca	15716	195010	8854	133167	13847	193121
Fe	111	853	143	1372	97	770
Br	1315	16964	813	12571	1262	17148
Sr	1234	9259	526	5456	1156	9227
I	642	3230	860	4325	1243	4053

Figure 3.2 suggest that there are higher concentrations for metals in the stationary coupons when compared to the dynamic flow coupons. This supports the preliminary assumptions because, when the flow is stationary, it allows for the other elements to compact onto the coupon's surface thus making it weigh slightly more than the dynamic flow coupons. It is important to note that the sodium content for the dynamic flow coupons had values that were too high to quantify; therefore, a value of 40,000 ng/mL was inputted for each week to accurately display the proposed amount of sodium present in the fracturing water. Sodium was the only element that had higher concentration values in the dynamic flow fracturing water when comparing it to the stationary fracturing water.

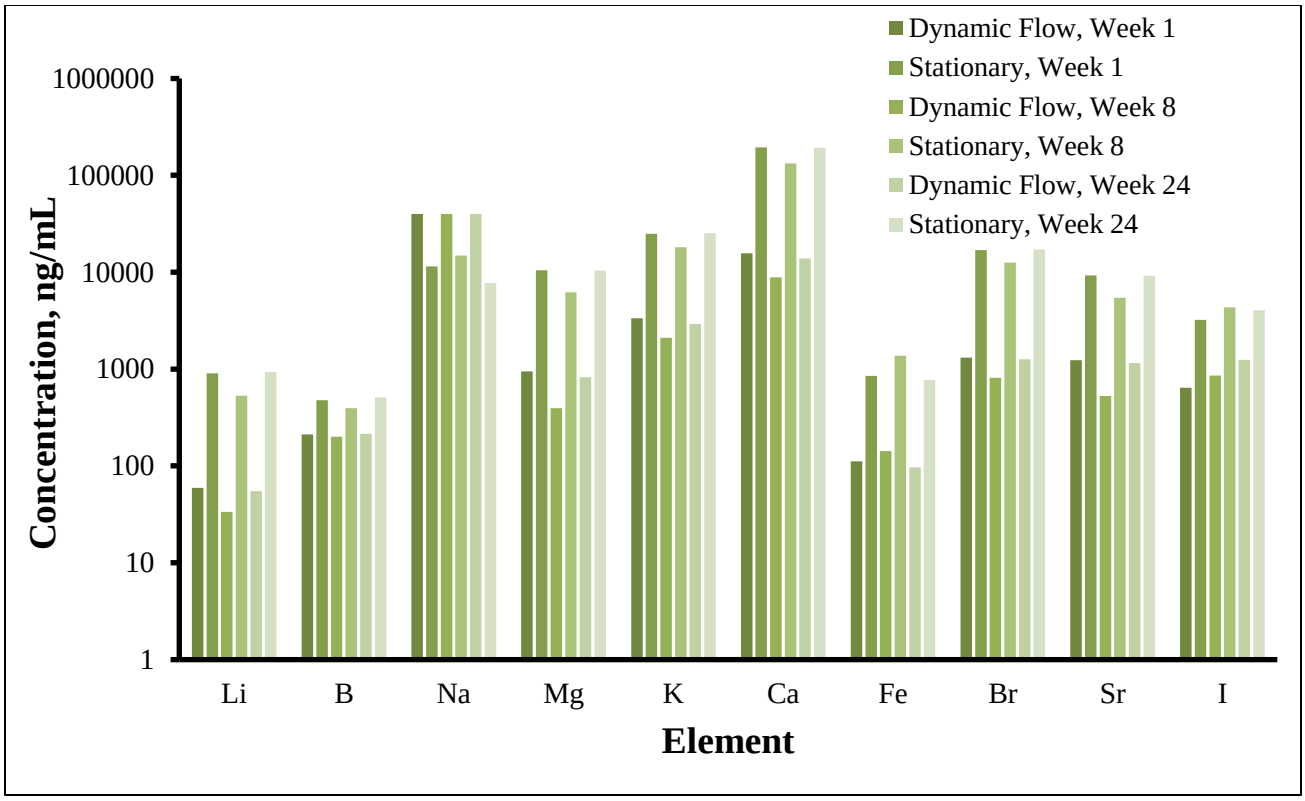

Figure 3.2 *The ICP-MS analysis for the dynamic flow and stationary coupons. From the graph, calcium was the major factor in mass changes for the coupons.*

3.3. Atomic Force Microscopy

Figures 3.3 through 3.11 are the images taken from the AFM. From observance, it was clear that the biofilms on stationary coupons formed a sharper and more exaggerated change than that of the untreated and dynamic flow coupons. The surface morphology of the dynamic flow coupons seemed to assemble a smoother surface. The flow around those coupons allowed for the biofilm to form a laminar boundary layer over the surface. This caused an even distribution on the coupons which led to the less dynamic changes in the surface. The untreated coupons, though not exposed to the fracturing water, also showed dynamic changes in the surface. Though this coupon corroded and decreased in weight, the surface seemed to get rougher over time.

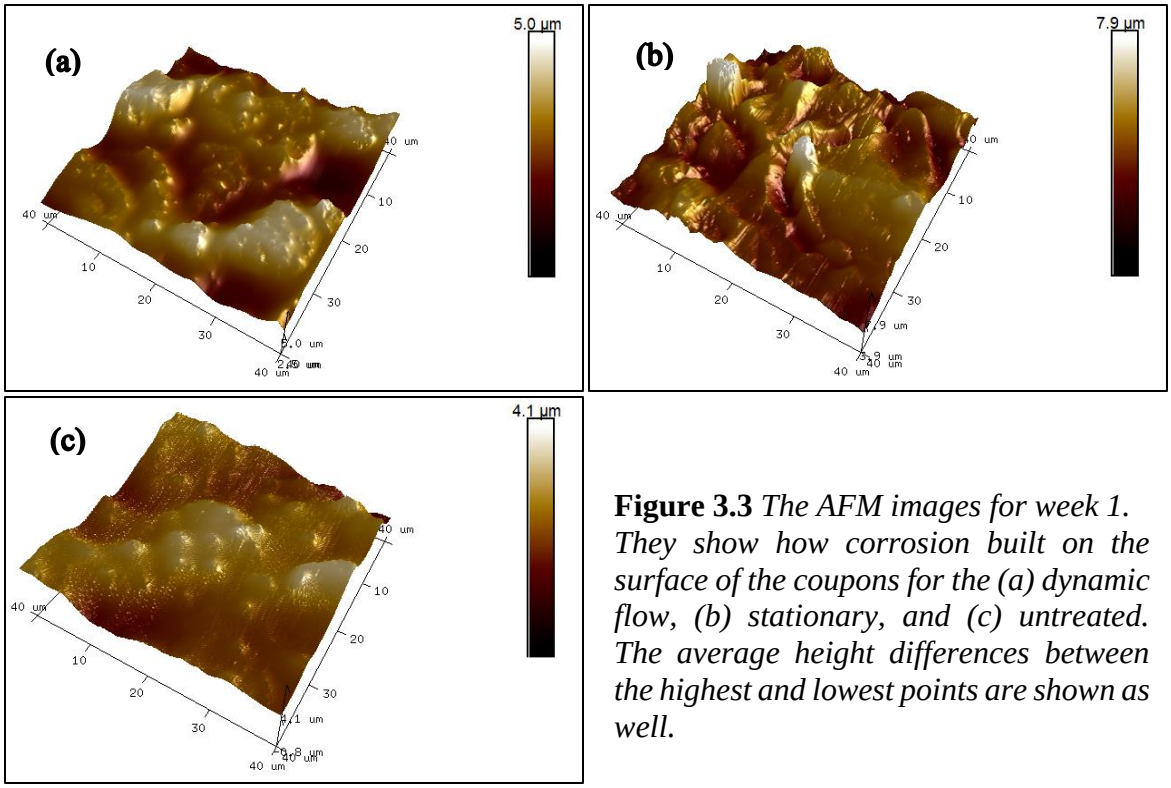

Figure 3.3 *The AFM images for week 1. They show how corrosion built on the surface of the coupons for the (a) dynamic flow, (b) stationary, and (c) untreated. The average height differences between the highest and lowest points are shown as well.*

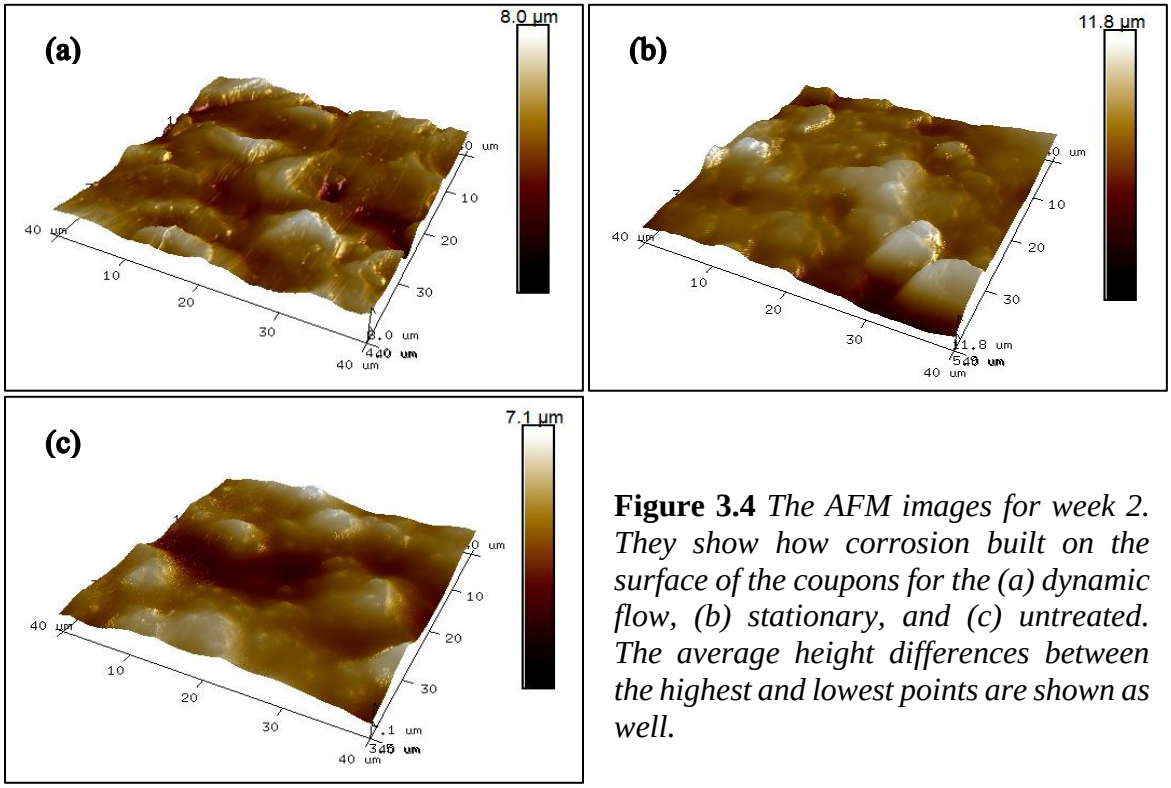

Figure 3.4 *The AFM images for week 2. They show how corrosion built on the surface of the coupons for the (a) dynamic flow, (b) stationary, and (c) untreated. The average height differences between the highest and lowest points are shown as well.*

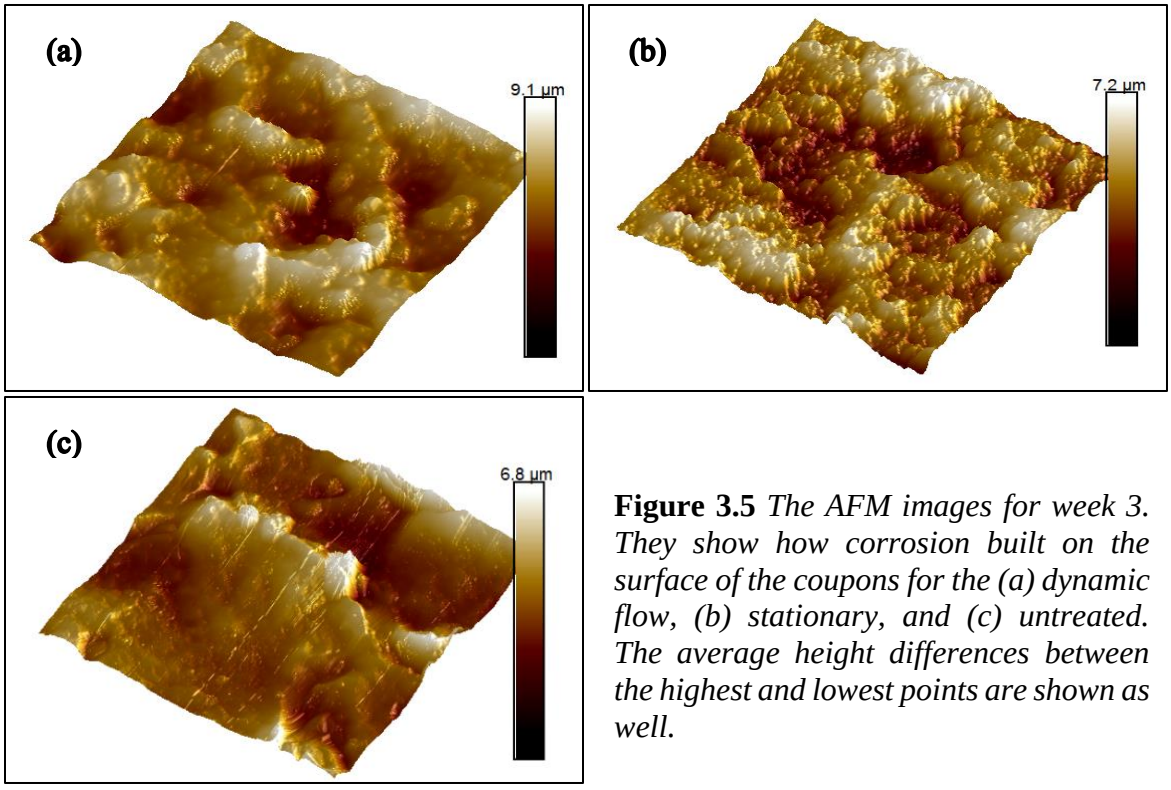

Figure 3.5 *The AFM images for week 3. They show how corrosion built on the surface of the coupons for the (a) dynamic flow, (b) stationary, and (c) untreated. The average height differences between the highest and lowest points are shown as well.*

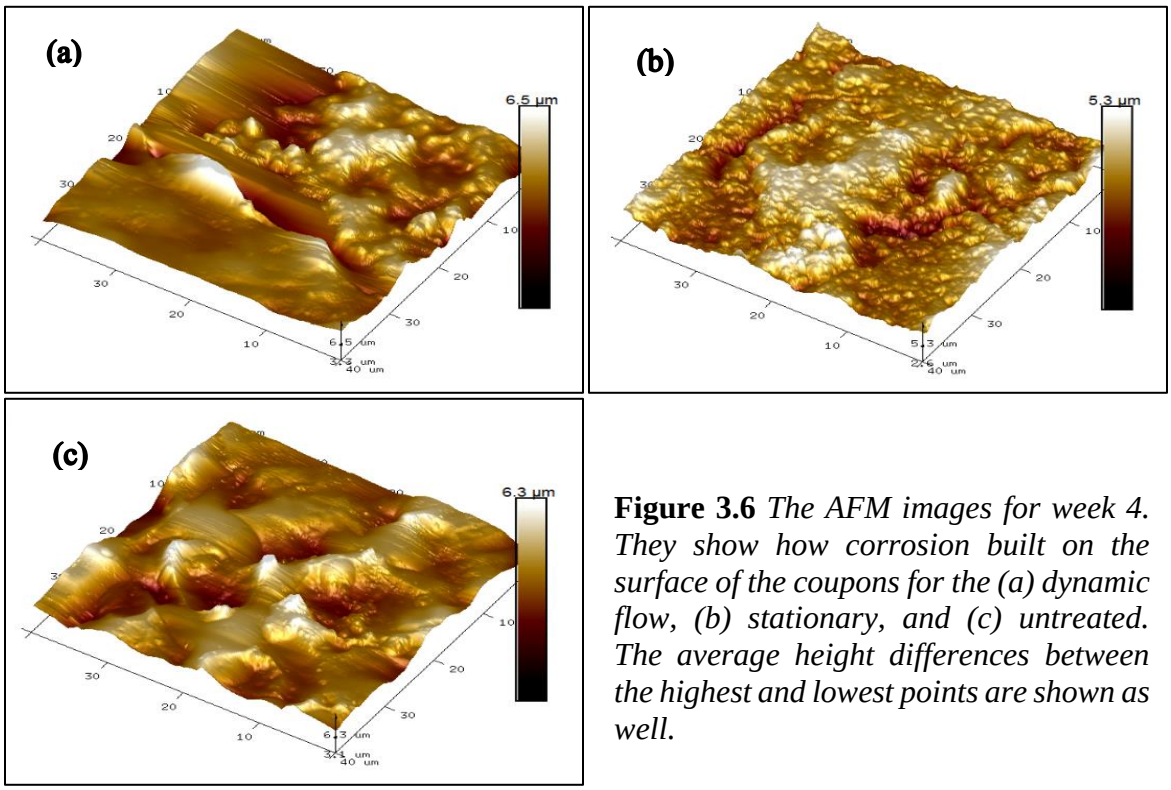

Figure 3.6 *The AFM images for week 4. They show how corrosion built on the surface of the coupons for the (a) dynamic flow, (b) stationary, and (c) untreated. The average height differences between the highest and lowest points are shown as well.*

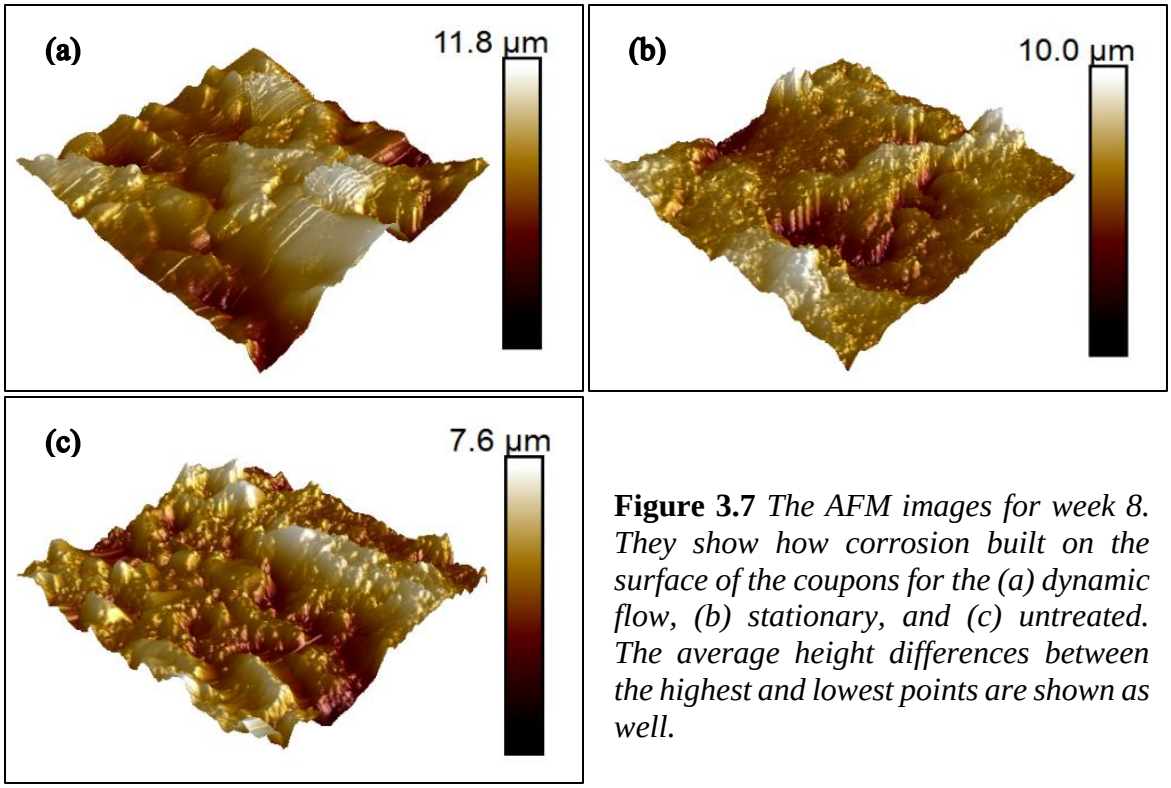

Figure 3.7 *The AFM images for week 8. They show how corrosion built on the surface of the coupons for the (a) dynamic flow, (b) stationary, and (c) untreated. The average height differences between the highest and lowest points are shown as well.*

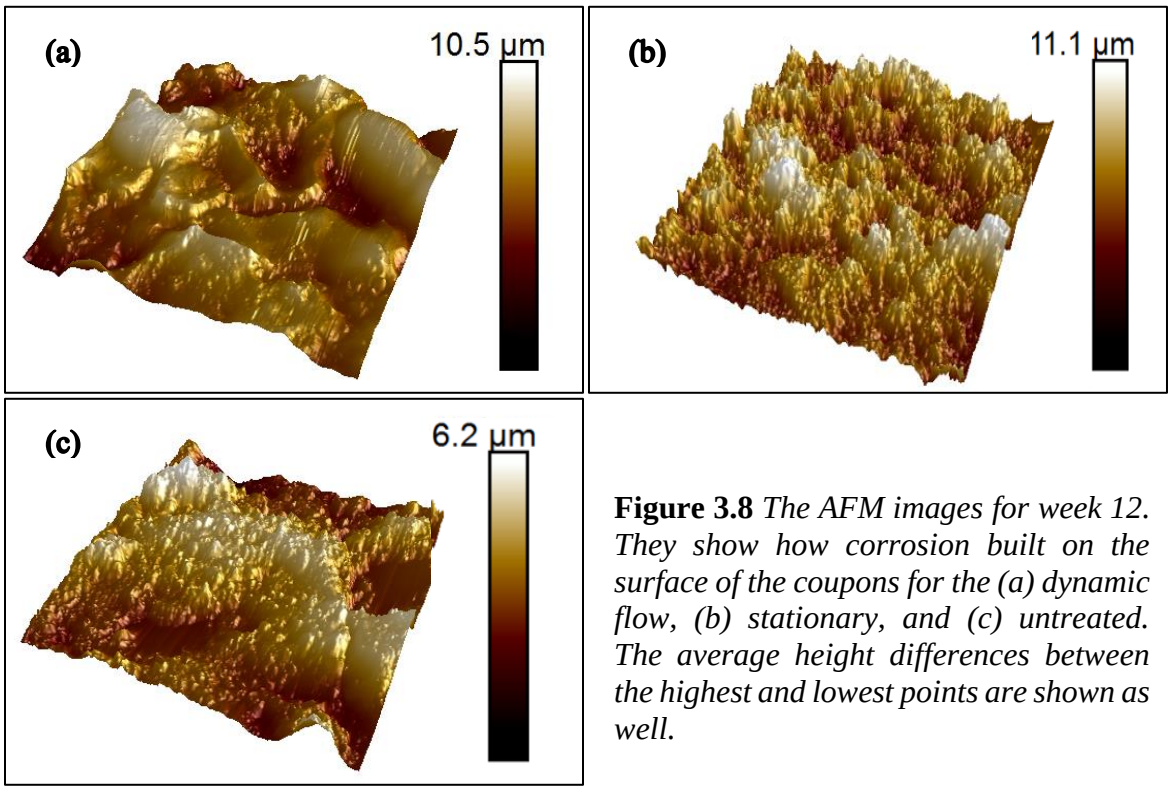

Figure 3.8 *The AFM images for week 12. They show how corrosion built on the surface of the coupons for the (a) dynamic flow, (b) stationary, and (c) untreated. The average height differences between the highest and lowest points are shown as well.*

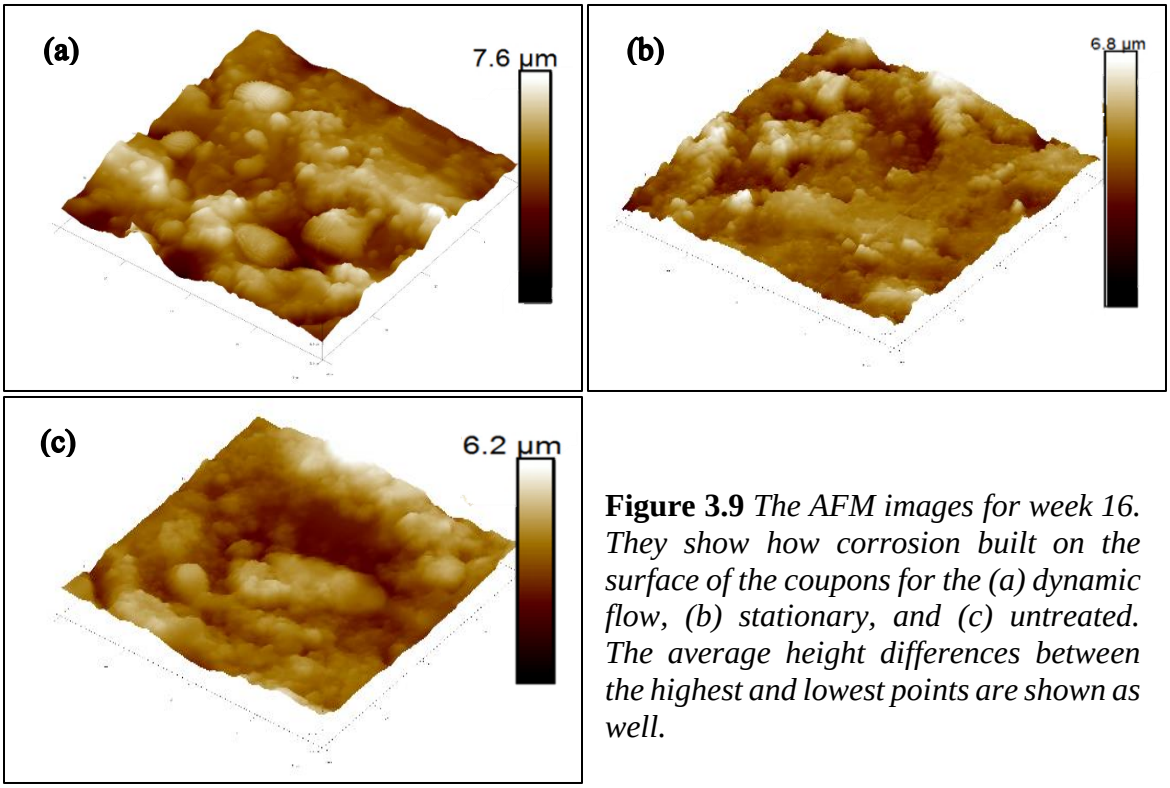

Figure 3.9 *The AFM images for week 16. They show how corrosion built on the surface of the coupons for the (a) dynamic flow, (b) stationary, and (c) untreated. The average height differences between the highest and lowest points are shown as well.*

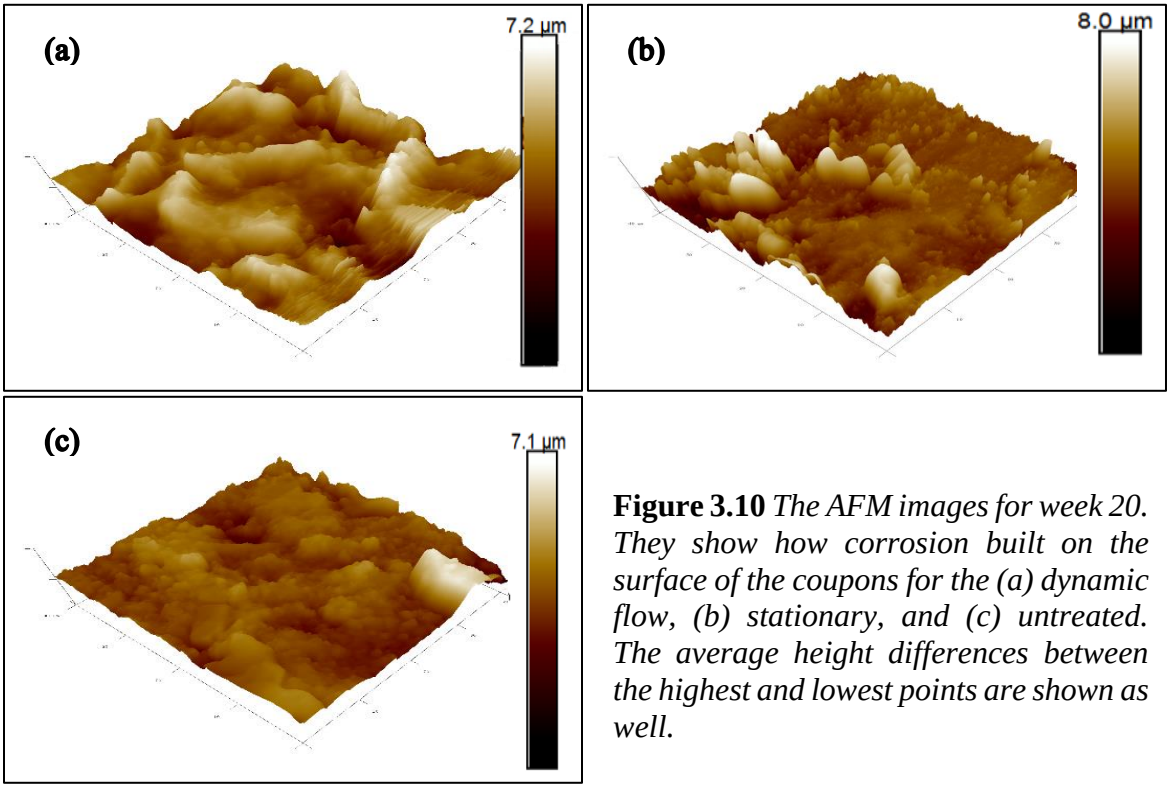

Figure 3.10 *The AFM images for week 20. They show how corrosion built on the surface of the coupons for the (a) dynamic flow, (b) stationary, and (c) untreated. The average height differences between the highest and lowest points are shown as well.*

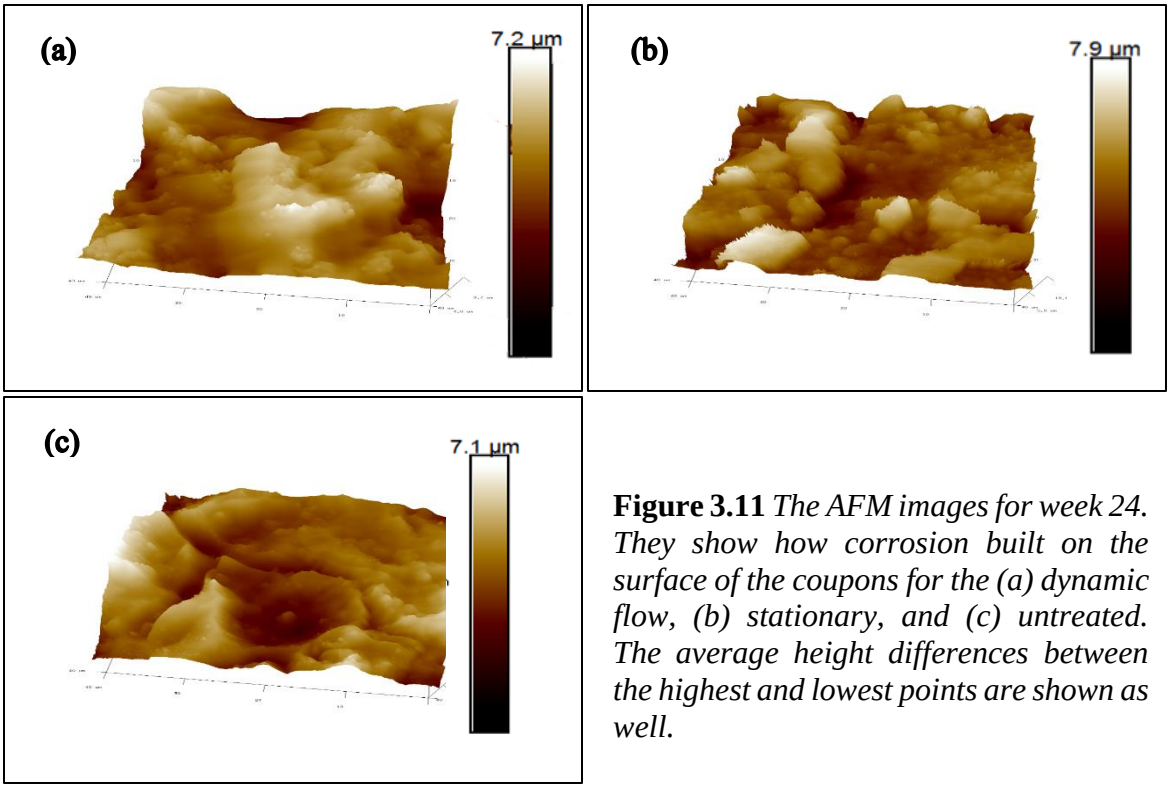

Figure 3.11 *The AFM images for week 24. They show how corrosion built on the surface of the coupons for the (a) dynamic flow, (b) stationary, and (c) untreated. The average height differences between the highest and lowest points are shown as well.*

Because the AFM produces images based off the surface roughness, statistical analysis was done in order to determine the skewness and kurtosis values for the surface morphology. Table 3.5 shows the values for the surface roughness for the untreated, dynamic flow, and stationary coupons. the dynamic flow coupons and the stationary coupons had higher values than the untreated samples. The roughness varied weekly, either increasing or decreasing.

Table 3.5 *Surface Roughness for Steel Coupons*

Week	Untreated (nm)	Flow (nm)	Stationary (nm)
Week 1	518	784	825
Week 2	546	909	1248
Week 3	598	1063	991
Week 4	661	872	786
Week 8	640	1105	1070
Week 12	676	1375	1394
Week 16	634	359	630
Week 20	701	674	899
Week 24	862	697	842

The skewness values for the untreated, dynamic flow, and stationary samples were 0.87, 0, and 0.53, respectively. Based on the analysis, the dynamic flow surface morphology had a Gaussian (normal) distribution because the curve is symmetrical. This supports its skewness value. The untreated and stationary coupons bother are moderately skewed to the right. This suggests that the surface roughness of these coupons was not as consistent for the experiment. This was interesting because the values for the untreated samples seemed to remain in close proximity, but the curve, Figure 3.12, proves its inconsistency.

Kurtosis assisted in categorizing the "central moment of profile amplitude probability density function" (Gadelmawla et al. 2002). The values for the kurtosis are 3.54 for untreated, 2.86 for the dynamic flow, and 2.33 for the stationary. The kurtosis value for the untreated samples is supported by the figure below because it has the sharpest peak of the three. A normal distribution value for kurtosis is 3. This means that the value for the dynamic flow supports it's the notion of normal distribution because the values if close to 3. The kurtosis for the stationary coupons was expected because of the unstable nature of the biofilm on their surface.

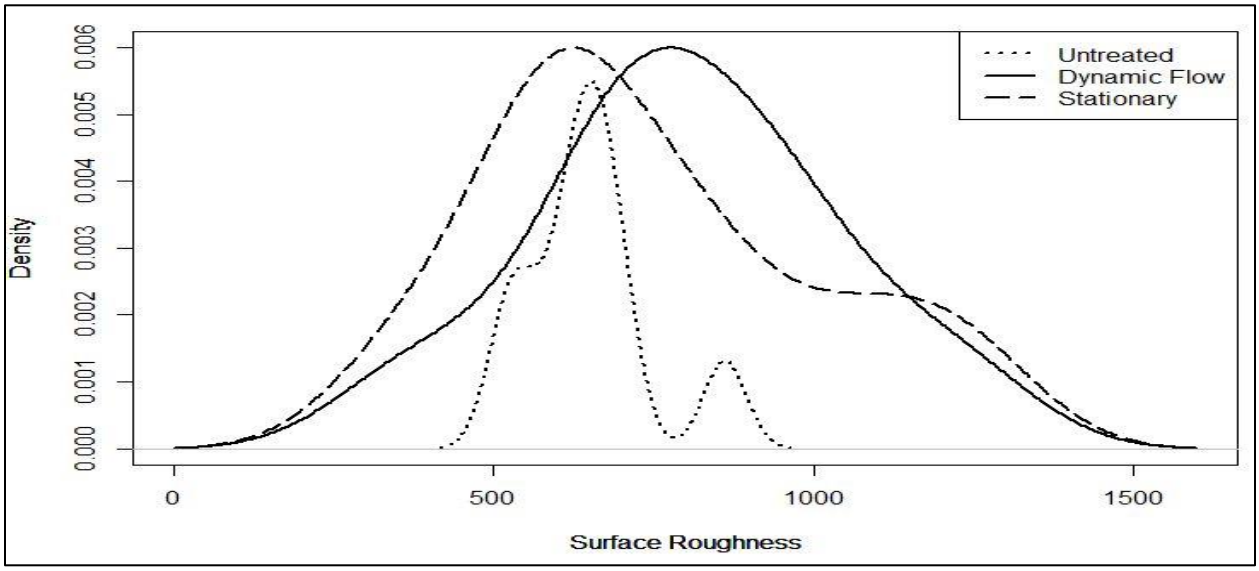

Figure 3.12 *The statistical analysis for the surface roughness. It shows skewness and kurtosis of the untreated, dynamic flow, and stationary coupons.*

3.4. ANSYS Workbench Simulation

The models below represent the process the steel coupons went through over the duration of the experiments. Each column shows the coupons in the respective environments. Through observation, the ANSYS models further supports the notion of the stationary coupons showing a more drastic change. It looks as though the biofilm is working its way to the middle of the dynamic flow coupons versus completely covering the surface as it is doing on the stationary coupons.

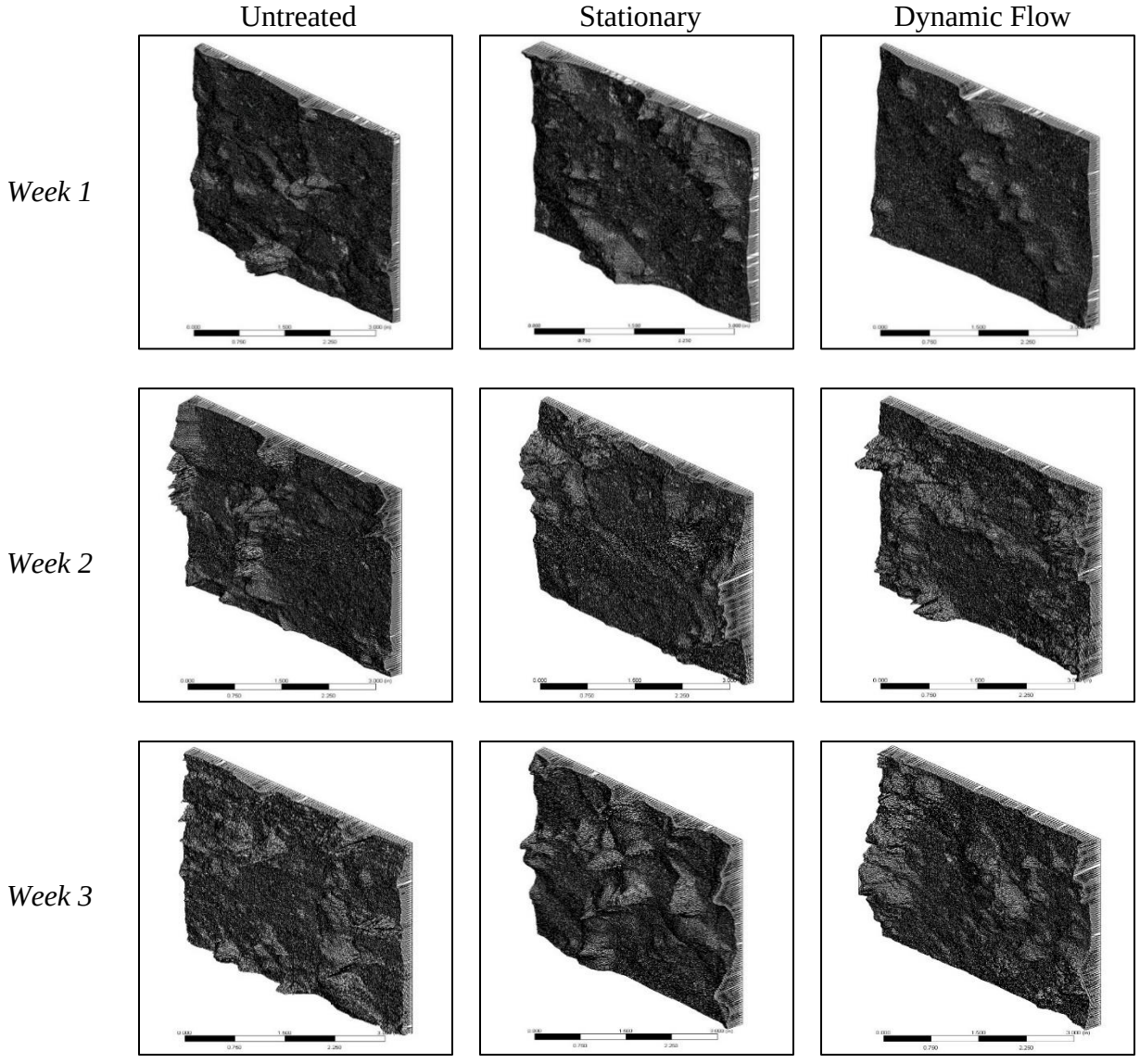

	Untreated	Stationary	Dynamic Flow
Week 4	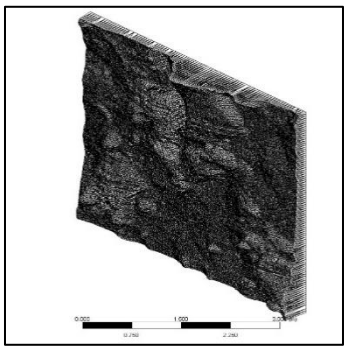	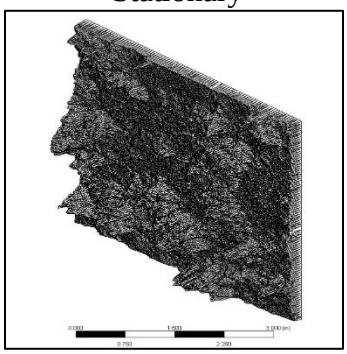	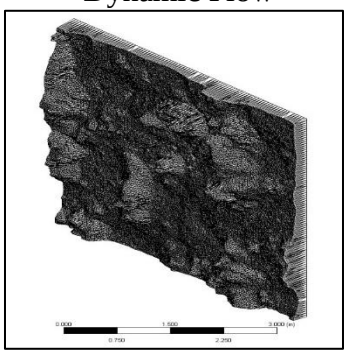
Week 8	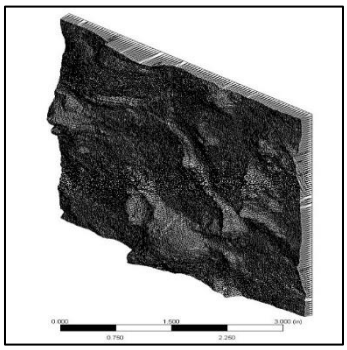	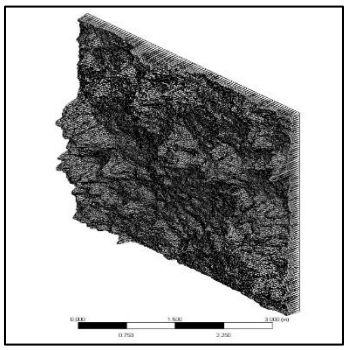	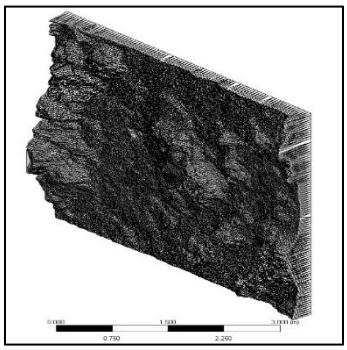
Week 12	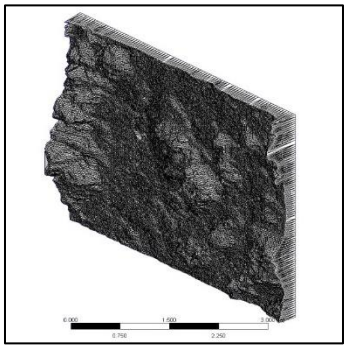	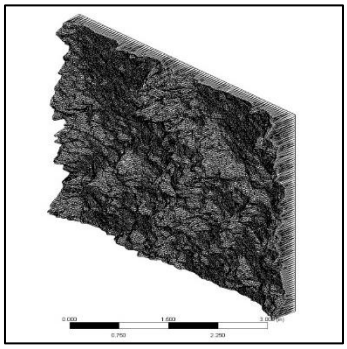	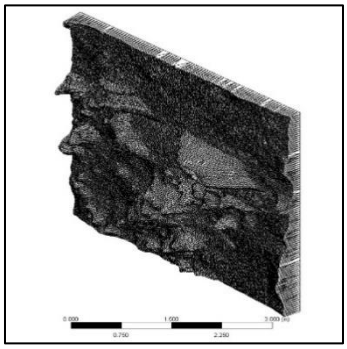
Week 16	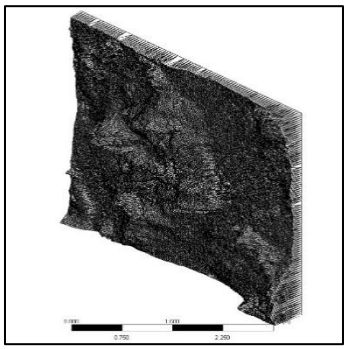	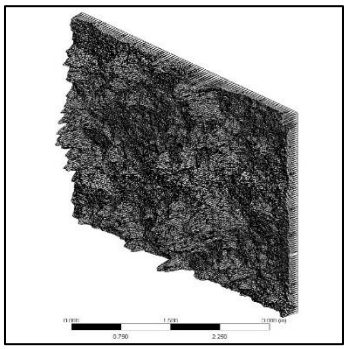	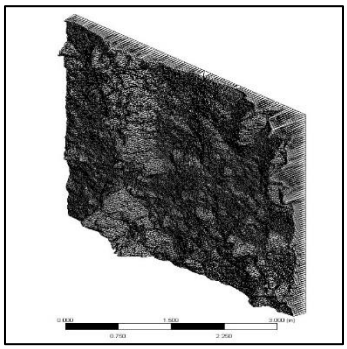

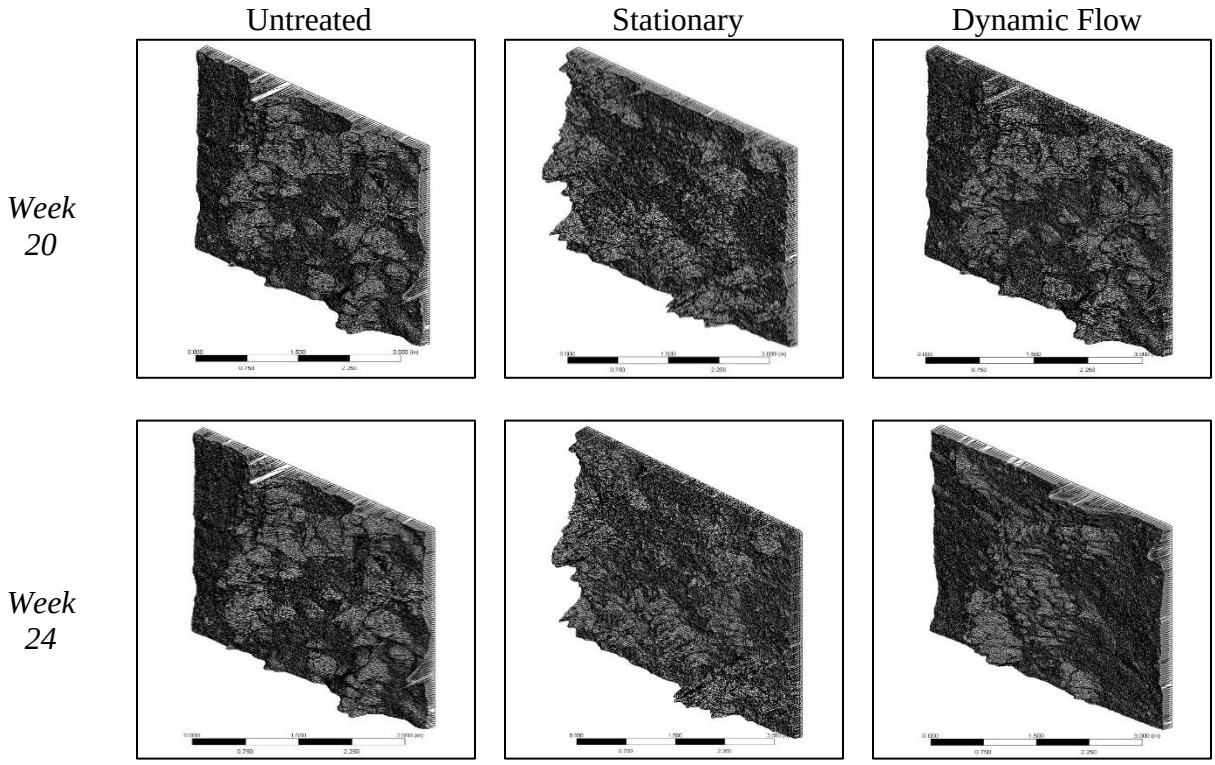

3.5. MATLAB Code

The sample MATLAB script below displays the code used to generate an animation for the steel coupons. This code was used for all coupons and combined the images from ANSYS to create the simulation. Using this code allowed for the creation of the predictive model necessary to determine how corrosion will build on the surface of the coupons. Notice that there are comments denoted by "%" to assist understanding what the code is doing at each point in the script.

```
% This code creates a video (default format of videos is .avi) from a compilation of images (default format of images is .jpg).
close all; clc; clear all;
%% Import the image files
Image_File_Directory = 'F:\Research Project\AFM Images\Flow\'; %Directory where images are contained, change to yours
First_Image = [Image_File_Directory '[insert image name here]_1.jpg']; %Specify first image, helps to keep these files sequentially ordered and numbered.
%%
video = VideoWriter('F:\Research Project\AFM Images\Flow', 'MPEG-4'); %create the video object, specify the video format here
```

```
video.FrameRate = 1; %This specifies the number of images per second. Must be called before "open"
%Call "open"
open(video); %open the file for writing
a=dir([Image_File_Directory '/*.jpg']);
N=size(a,1);
Height = 720;
Width = 1280;
for ii=1:N %where N is the number of images
   image = ['[insert image name here]_' num2str(ii)];
   I = imread([Image_File_Directory image '.jpg']); %read the next image
   J = imresize(I,[Height Width]);
   writeVideo(video,J); %write the image to file
   %One way of forcing the loop
%    img = [Image_File_Directory 'Image_Name_' num2str(ii) '.jpg'];
%    I = imread('img.jpg'); %read the next image
%    writeVideo(video,I); %write the image to file
end
close(video); %close the file
```

3.6. DNA Extraction Results

In Table 3.6, the values for the DNA concentrations are given. Based on the results, the amount of DNA on the samples showed a gradual increase and then begins to decrease.

Table 3.6 *DNA Extraction for Dynamic Flow and Stationary Coupons*

Week	Coupon Type	Concentration (ng/µl)	A260/A280	Total amount, ng
1	Stationary	1.2	1.51	60
1	Dynamic Flow	0.7	1.56	35
2	Stationary	1.7	1.39	85
2	Dynamic Flow	3.1	1.36	155
3	Stationary	4.0	1.28	200
3	Dynamic Flow	0.6	2.13	30
4	Stationary	0.4	0.73	20
4	Dynamic Flow	1.1	1.76	55
8	Stationary	7.0	1.27	350
8	Dynamic Flow	1.9	1.42	95
12	Stationary	0.1	1.42	5
12	Dynamic Flow	0.6	1.89	30
16	Stationary	0.6	2.08	30
16	Dynamic Flow	0.6	1.81	30

Figure 3.13 shows the DNA extraction results for the biofilm developed in this study. The trend of the DNA sequencing supports all of the results that have been obtained from the experiments. The biofilm DNA shows a gradual build over time, and once it reaches its plateau, the DNA begins to salt of the surface of the coupons.

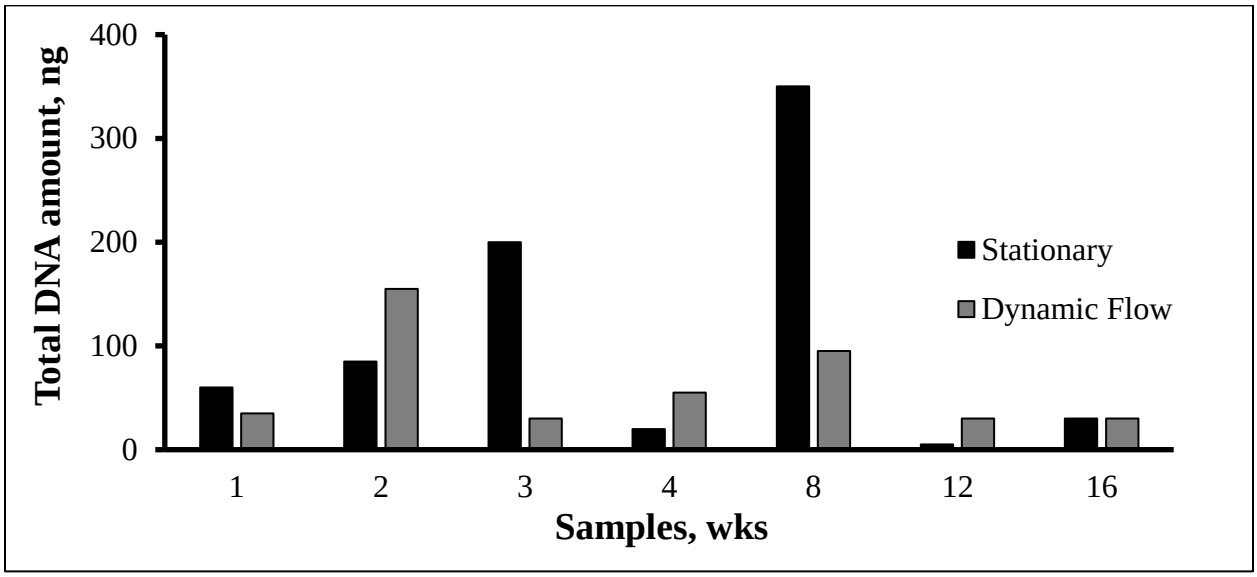

Figure 3.13 *The DNA extraction results from the biofilm. From the graph, it can be seen that the stationary flow coupons had higher amounts on DNA in its biofilms' development.*

3.7. Illumina Sequencing Results

Figure 3.14 shows the fracturing water microbiome composition. The archaea *Methanolobus* (highest percentage, 34.3%) is a coccoid methanogen growing only on methanol and methylamines. *Bacteroides luti* sp. *nov*., (10.5%) an anaerobic, cellulolytic and xylanolytic bacterium isolated from methanogenic sludge. An unusual Arcobacter species, designated strain CAB (8.9%), was isolated from marine sediment and found to have the capacity to grow via perchlorate reduction, the only member of the epsilonproteobacteria in pure culture to possess this rare metabolism. Oceanospirillaceae (6.7%) are hydrocarbon degraders, enriched by crude oil. Oceanospirillaceae (6.7%), Marinobacterium (1.9%), Schewanella (0.1%) belong to

gammaproteobacteria taxa that are known hydrocarbon degraders and become enriched in the presence of crude oil.

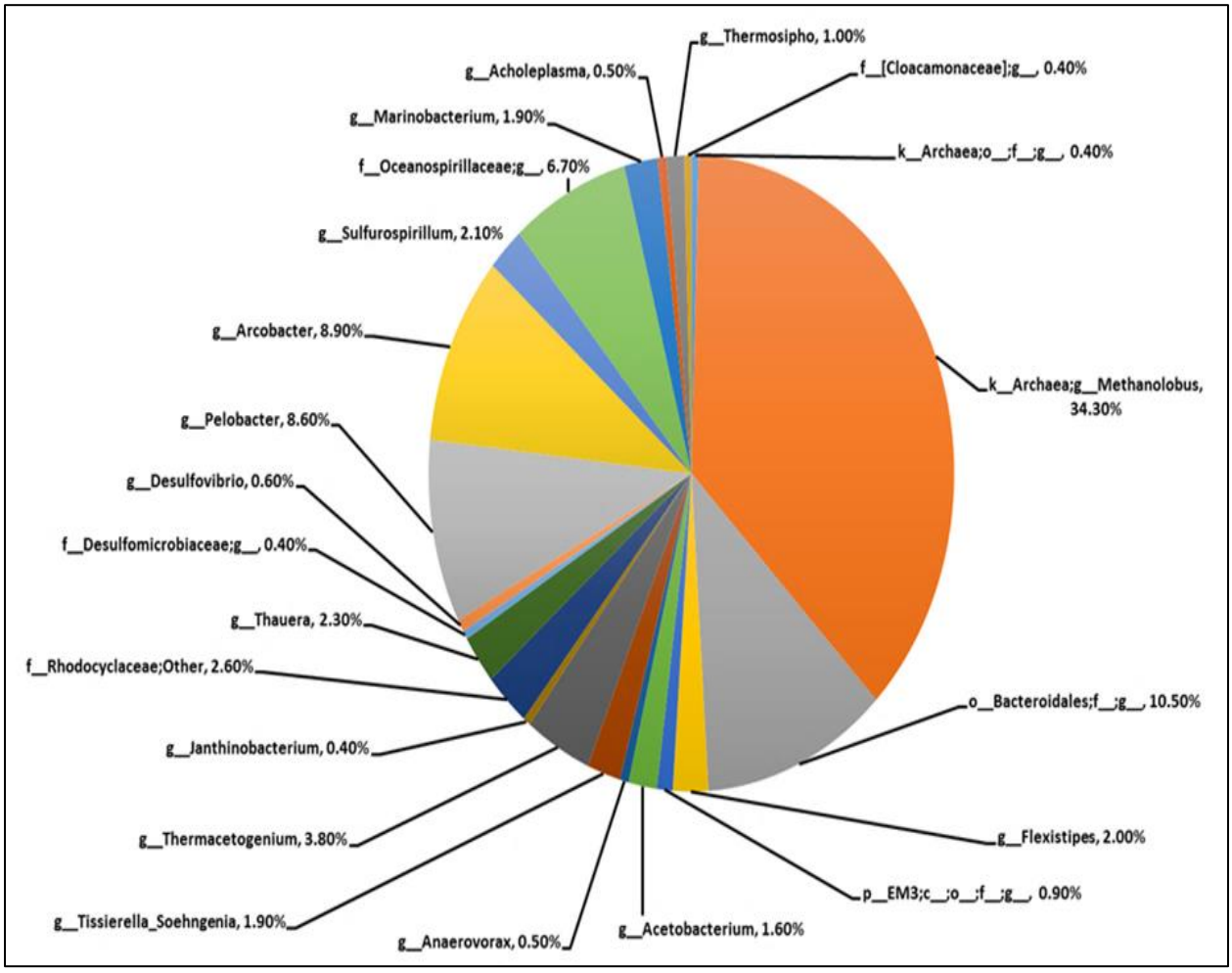

Figure 3.14 *Illumina Sequencing of the fracturing water microbiome composition.*

3.8. Kinetics

The experimental kinetics were taken for three different periods−the beginning, middle and end. This analysis was based upon the assumption that the specified time frames would contain the critical values for the rate of detachment. Table 3.7 displays the computed data for the net biofilm production rate, the deposition rate, detachment rate, and the attached biofilm rate.

Table 3.7 *Numerical Values of Attached Biofilm Rates*

Stationary				
Rate Type	Net Biofilm Production	Deposition	Detachment	Attached Biofilm
Week 1	9.0E-2	4.0E-2	5.1E-3	1.3E-1
Week 8	2.3E-1	5.2E-3	7.0E-4	2.3E-1
Week 24	7.3E-2	1.5E-3	1.9E-4	7.4E-2
Dynamic Flow				
Rate Type	Net Biofilm Production	Deposition	Detachment	Attached Biofilm
Week 1	2.1E-1	3.2E-3	6.9E-4	2.1E-1
Week 8	1.3E-1	3.4E-4	8.2E-5	1.3E-1
Week 24	5.2E-2	1.0E-4	2.2E-5	5.2E-2

From Figure 3.15, it can be seen that the attached biofilm rate for the dynamic flow coupons constantly decreased while the stationary coupons fluctuated. Ultimately, the rate started off higher for the biofilm on the dynamic flow coupons and then became smaller than the biofilm on the stationary coupons. This supports the data from experimentation because higher detachment rates cause the biofilm to disperse at a slower pace.

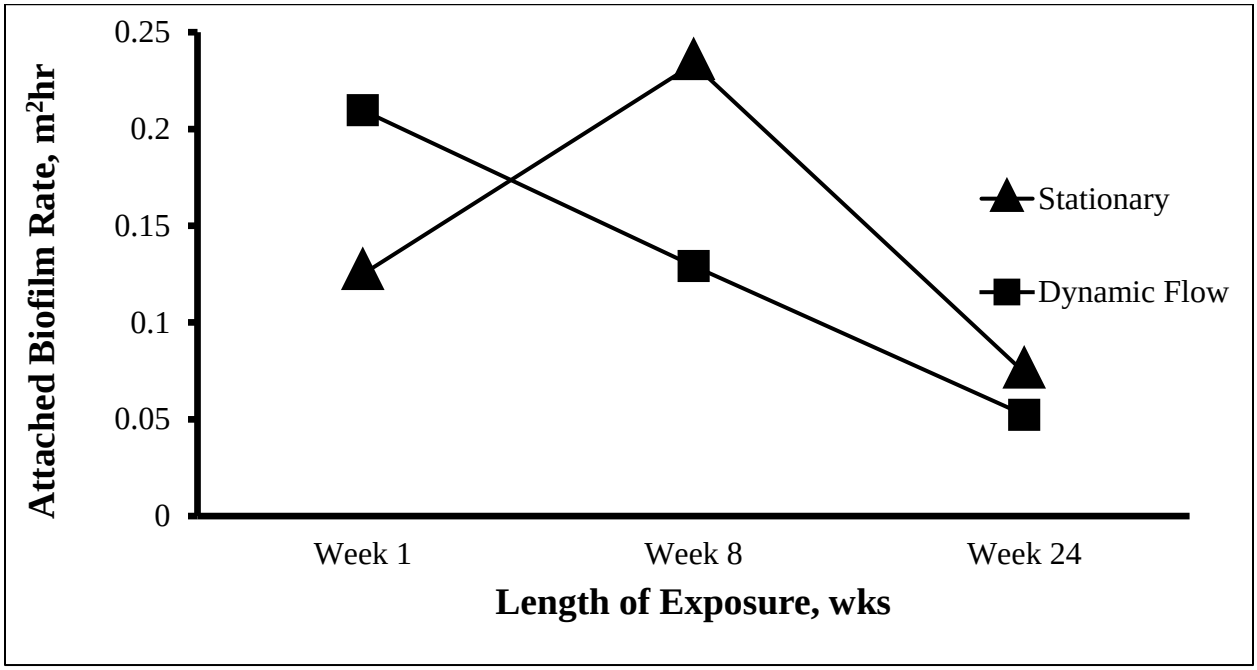

Figure 3.15 *The attached biofilm rate. It shows the rate at which the biofilm was attaching itself to the surface of the coupons.*

3.9. Corrosion Rate Comparison

It was assumed that the stationary coupons would corrode the quickest over time through preliminary analysis and measurements. The corrosion rate was determined every week, and this was held true for every experiment. From Figure 3.16, it is clear that the longer the coupons were being exposed to heat and fracturing water, the faster they would corrode. The dynamic flow coupons do corrode at rapid rate as well, but because the weight changes were slightly smaller than the weight of the stationary coupons, it caused the estimate for corrosion to be lower. Though weight is directly related to the corrosion rate, time exposure is indirectly related, so the data makes sense.

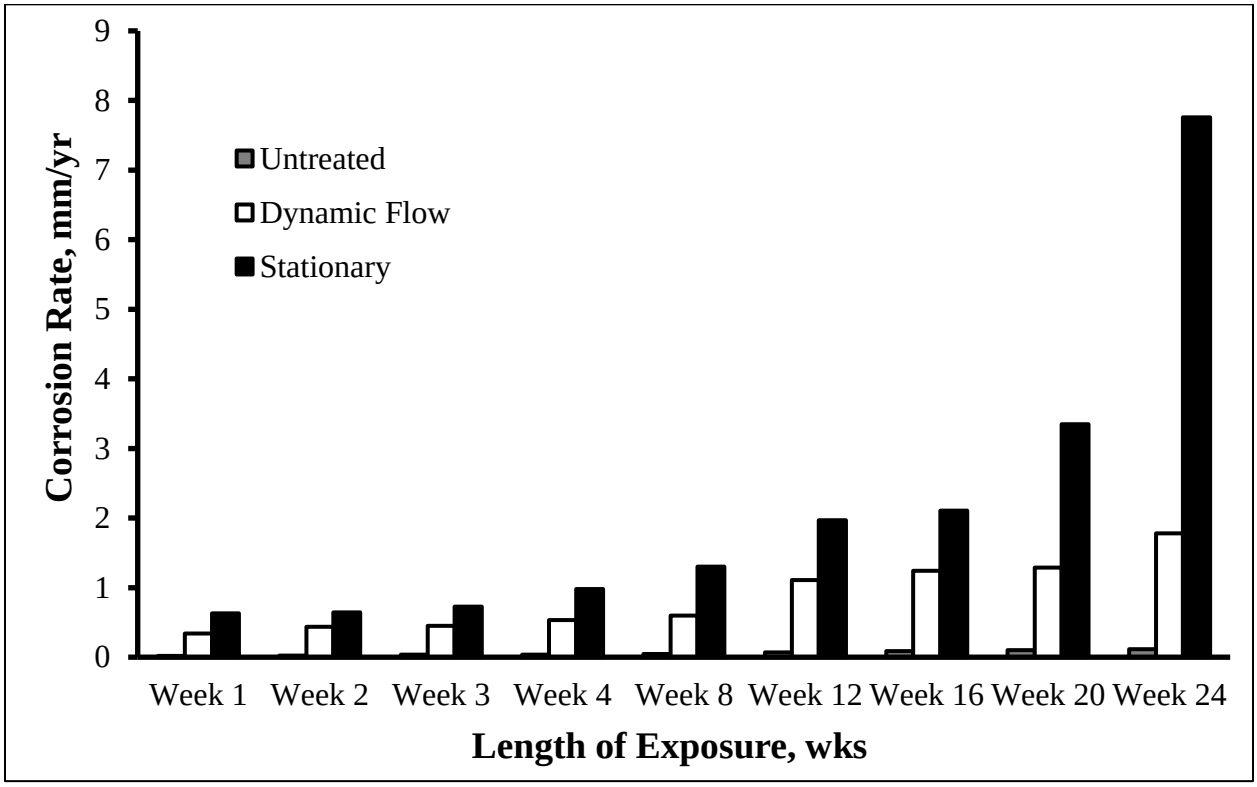

Figure 3.16 *The corrosion rate comparison for all coupons. The graph shows the results for the untreated, dynamic flow, and stationary samples.*

4. CONCLUSIONS

4.1. Conclusions

This study has described, in detail, the processes and methods needed to further corrosion studies and biofilm formation. This experiment gave a thorough analysis of dynamic biofilm growth and how it forms on the surface of steel alloys. The simulations assisted in narrowing corrosion inhibitor techniques and preferences by establishing a basis to forecast how biofilms will form on steel equipment based on the surrounding environment. This research was essential because it will diminish corrosion failures in the oil industry and will inherently reduce economic losses. The successful application of these methods enabled for the development of a structured process for solving corrosion problems. The primary focus was to fill a gap in corrosion studies.

In conclusion, this research study is expected to be beneficial to the oil industry while also being applicable to many other production fields as well. In regards to corrosion rate, the coupons in a stationary state are expected to deteriorate the quickest based upon the results of the experiments. Its average corrosion rate for the experiments was over 2 mm per year which is more than double of the average corrosion rate of the dynamic flow coupons and untreated. Therefore, it is recommended to keep steel equipment in a flow with fluid in order to extend its use.

4.2. Recommendations

For future work, the experiment should be run with more dynamic conditions such as a higher temperature of the heating chamber, higher flow velocity, and a higher pressure. Also, this experiment could be run on different metals such as copper, nickel, or chromium and the results could be compared to those of the stainless steel. This would help in predicting what metal is least susceptible to corrosion. I recommend that this experiment also be ran with a corrosion inhibitor to determine if there would be any changes in the results or data trends.

REFERENCES

(2002). “Corrosion Costs and Preventive Strategies in the United States,” *NACE International*.

Baker, G. C., Smith, J. J., & Cowan, D. A. (2003). “Review and re-analysis of domain-specific 16S primers,” *Journal of Microbiological Methods, 55*(3), 541-555. https://doi.org/10.1016/j.mimet.2003.08.009

Bryers, J. D., & Characklis, W. G. (1982). “Processes governing primary biofilm formation,” *Biotechnology and Bioengineering*, 24(11), 2451–2476. https://doi: 10.1002/bit.260241111

Cadieux, P., Wignall, G., Carriveau, R., & Denstedt, J. (2008). “Implications of Biofilm Formation on Urological Devices,” *AIP Conference Proceedings*, 1049(1). https://doi.org/10.1063/1.2998011

Caporaso, J. G., Kuczynski, J., Stombaugh, J., Bittinger, K., Bushman, F. D., Costello, E. K., & Knight, R. (2010). “QIIME allows analysis of high-throughput community sequencing data,” *Nature Methods, 7*(5), 335-336. https://doi.org/10.1038/nmeth.f.303

Clark, J. (1949). "A Hydraulic Process for Increasing the Productivity of Wells," *Journal of Petroleum Technology*, vol. 1. https://doi.org/10.2118/949001-G

Donlan, M. R. (2002). “Biofilms: Microbial Life on Surfaces,” *Emerging Infectious Diseases*, 8(9), pp. 881-890. https://dx.doi.org/10.3201/eid0809.020063

Eckert, R. B. (2015). “Emphasis on biofilms can improve mitigation of microbiologically influenced corrosion in oil and gas industry,” *Corrosion Engineering, Science and Technology*, 50(3), pp. 163-168, DOI: 10.1179/1743278214Y.0000000248

Gadelmawla, E. S., Koura, M.M., Maksoud, T. M. A., Elewa, I. M., & Soliman, H. H. (2002). “Roughness parameters,” *Journal of Materials Processing Technology*, 123(1), pp. 133-145, https://doi.org/10.1016/S0924-0136(02)00060-2

Gavara N. (2017). “A beginner's guide to atomic force microscopy probing for cell mechanics,” *Microscopy research and technique*, 80(1), pp. 75–84. https://doi.org/10.1002/jemt.22776

Hakkarainen, T. J. (2003). “Microbiologically influenced corrosion of stainless steels – What is required for pitting?,” *Materials and Corrosion*, 54(7), pp. 503-509. https://doi.org/10.1002/maco.200390112

Lewandowski, Zbigniew, & Beyenal, Haluk. (2003). “Biofilm monitoring: A perfect solution in search of a problem,” *Water science and technology: A journal of the International Association on Water Pollution Research,* 47(5). 9-18. https://doi.org/10.2166/wst.2003.0267.

Nanan, K. (2018). “Pitting Corrosion in Oil and Gas Wells and Pipelines,” *Oilman Magazine*.

Peszynska,M., Trykozko, A., Iltis, G., Schlueter, S., & Wildenschild, D. (2016). “Biofilm growth in porous media: Experiments, computational modeling at the porescale, and upscaling,” *Advances in Water Resources,* vol. 95, pp. 288-301. https://doi.org/10.1016/j.advwatres.2015.07.008

Popoola, L.T., Grema, A.S., Latinwo, G.K., Gutti, B., & Saheed, A. (2013). “Corrosion problems during oil and gas production and its mitigation,” *International Journal of Industrial Chemistry 4*, 35. https://doi.org/10.1186/2228-5547-4-35

Ravindran, P. (2016). “Nanomaterials Synthesis: Soft Lithography,” *Nanomaterials and Nanotechnology.* http://folk.uio.no/ravi/cutn/nmnt/13.Nanomaterials_synthesis-2.pdf

Umeozokwere, O, Mbabuike, U, Oreko, Benjamin, & Ezemuo D.T. (2016). “Corrosion Rates and its Impact on Mild Steel in Some Selected Environments,” *The Journal of Scientific and Engineering Research*, vol. 3, pp. 34-43.

Uruba, Vaclav. (2018). “On Reynolds number physical interpretation,” *AIP Conference Proceedings 2000*. 020019. https://doi.org/10.1063/1.5049926

Vishalashi, R. (2017). “Application of Hooks Law in Elasticity,” *Paripex – Indian Journal of Research*, 6(11), pp. 545-547.

Wang, Y., & Qian, P.-Y. (2009). “Conservative fragments in bacterial 16S rRNA genes and primer design for 16S ribosomal DNA amplicons in metagenomic studies,” *PLOS One, 4*(10), e7401. https://doi.org/10.1371/journal.pone.0007401

Yari, M. (2017). “The 6 Corrosive Components That Can Be Found in Crude Oil,” *Corrosionpedia*.

Zhang, D., Zhou, F., Xiao, K., Cui, T., Qian, H., & Li, X. (2015). “Microbially Influenced Corrosion of 304 Stainless Steel and Titanium by P. variotii and A. niger in Humid Atmosphere,” *Journal of Materials Engineering and Performance*, pp. 2688-2698. https://doi.org/10.1007/s11665-015-1558-2

Zhou, C., Yang, Y., & Jong, A. Y. (1990). “Mini-prep in ten minutes’” *Biotechniques, 8*(2), 172-173.

APPENDIX A

MATLAB CODE FOR THE ANIIMATION OF THE COUPONS

```
%% Matlab Video Creator
% This code creates a video (default format of videos is .avi) from a
% compilation of images (default format of images is .jpg).
close all; clc; clear all;

%% Import the image files
Image_File_Directory = 'F:\Research Project\AFM Images\Untreated\'; %Directory where images are contained, change to yours
First_Image = [Image_File_Directory 'untreated_1.jpg']; %Specify first image, helps to keep these files sequentially ordered and numbered.
%%

video = VideoWriter('F:\Research Project\AFM Images\Untreated', 'MPEG-4'); %create the video object, specify the video format here
video.FrameRate = 1; %This specifies the number of images per second. Must be called before "open"
%Call "open"
open(video); %open the file for writing

a=dir([Image_File_Directory '/*.jpg']);
N=size(a,1);
Height = 720;
Width = 1280;
for ii=1:N %where N is the number of images
    image = ['untreated_' num2str(ii)];
    I = imread([Image_File_Directory image '.jpg']); %read the next image
    J = imresize(I,[Height Width]);
    writeVideo(video,J); %write the image to file

    %One way of forcing the loop
%    img = [Image_File_Directory 'Image_Name_' num2str(ii) '.jpg'];
%    I = imread('img.jpg'); %read the next image
%    writeVideo(video,I); %write the image to file
end

close(video); %close the file
```

Untreated Code

Link to Animation: https://figshare.com/s/5493951eb58f158b4b30

```
%% Matlab Video Creator
% This code creates a video (default format of videos is .avi) from a
% compilation of images (default format of images is .jpg).
close all; clc; clear all;

%% Import the image files
Image_File_Directory = 'F:\Research Project\AFM Images\Stationary\'; %Directory where images are contained, change to yours
First_Image = [Image_File_Directory 'stationary_1.jpg']; %Specify first image, helps to keep these files sequentially ordered and numbered.
%%

video = VideoWriter('F:\Research Project\AFM Images\Stationary', 'MPEG-4'); %create the video object, specify the video format here
video.FrameRate = 1; %This specifies the number of images per second. Must be called before "open"
%Call "open"
open(video); %open the file for writing

a=dir([Image_File_Directory '/*.jpg']);
N=size(a,1);
Height = 720;
Width = 1280;
for ii=1:N %where N is the number of images
    image = ['stationary_' num2str(ii)];
    I = imread([Image_File_Directory image '.jpg']); %read the next image
    J = imresize(I,[Height Width]);
    writeVideo(video,J); %write the image to file

    %One way of forcing the loop
%    img = [Image_File_Directory 'Image_Name_' num2str(ii) '.jpg'];
%    I = imread('img.jpg'); %read the next image
%    writeVideo(video,I); %write the image to file
end

close(video); %close the file
```

Stationary Code

Link to Animation: https://figshare.com/s/bd4c08d7219b78168311

```
%% Matlab Video Creator
% This code creates a video (default format of videos is .avi) from a
% compilation of images (default format of images is .jpg).
close all; clc; clear all;

%% Import the image files
Image_File_Directory = 'F:\Research Project\AFM Images\Flow\'; %Directory where images are contained, change to yours
First_Image = [Image_File_Directory 'flow_1.jpg']; %Specify first image, helps to keep these files sequentially ordered and numbered.
%%

video = VideoWriter('F:\Research Project\AFM Images\Flow', 'MPEG-4'); %create the video object, specify the video format here
video.FrameRate = 1; %This specifies the number of images per second. Must be called before "open"
%Call "open"
open(video); %open the file for writing

a=dir([Image_File_Directory '/*.jpg']);
N=size(a,1);
Height = 720;
Width = 1280;
for ii=1:N %where N is the number of images
    image = ['flow_' num2str(ii)];
    I = imread([Image_File_Directory image '.jpg']); %read the next image
    J = imresize(I,[Height Width]);
    writeVideo(video,J); %write the image to file

    %One way of forcing the loop
%    img = [Image_File_Directory 'Image_Name_' num2str(ii) '.jpg'];
%    I = imread('img.jpg'); %read the next image
%    writeVideo(video,I); %write the image to file
end

close(video); %close the file
```

Dynamic Flow Code

Link to Animation: https://figshare.com/s/b951a2bc34c134adbbe9